A&A 546, A65 (2012)
DOI: 10.1051/0004-6361/201219318

Astronomy & Astrophysics

Multiwavelength analysis of the Lyman-α emitting galaxy Haro 2: relation between the diffuse Lyman-α and soft X-ray emissions

H. Otí-Floranes[1,2], J. M. Mas-Hesse[1], E. Jiménez-Bailón[3], D. Schaerer[4,5], M. Hayes[6,5], G. Östlin[7], H. Atek[8], and D. Kunth[9]

[1] Centro de Astrobiología (INTA–CSIC), Departamento de Astrofísica, POB 78, 28691 Villanueva de la Cañada, Spain
e-mail: [otih;mm]@cab.inta-csic.es
[2] Dpto. de Física Moderna, Facultad de Ciencias, Universidad de Cantabria, 39005 Santander, Spain
[3] Instituto de Astronomía, Universidad Nacional Autónoma de México, Apartado Postal 70-264, 04510 México DF, México
[4] Observatoire de Genève, Université de Genève, 51 Ch. des Maillettes, 1290 Versoix, Switzerland
[5] CNRS, Institut de Recherche en Astrophysique et Planétologie, 14 avenue Edouard Belin, 31400 Toulouse, France
[6] Université de Toulouse, UPS-OMP, IRAP, 31028 Toulouse, France
[7] Department of Astronomy, Oskar Klein Centre, Stockholm University, 106 91 Stockholm, Sweden
[8] Spitzer Science Center, Caltech, Pasadena, CA 91125, USA
[9] Institut d'Astrophysique de Paris, UMR 7095 CNRS & UPMC, 98bis Bd Arago, 75014 Paris, France

Received 30 March 2012 / Accepted 30 July 2012

ABSTRACT

Context. Lyman-α emission is commonly used as star formation tracer in cosmological studies. Nevertheless, resonant scattering strongly affects the resulting luminosity, leading to variable and unpredictable escape fractions in different objects.
Aims. To understand how the Lyα escape fraction depends on the properties of the star-forming regions, we need high spatial resolution multiwavelength studies of nearby Lyα emitters, like Haro 2.
Methods. We study the Lyα emission of Haro 2 in connection with the properties of the young stellar population, the characteristics of the interstellar medium, the distribution and intensity of the Balmer emission lines and the properties of the X-ray emission. We have used HST-STIS spectral images along the major and minor axes of Haro 2 to characterize the Lyα emission, as well as FOC UV, WFPC-2 optical and NICMOS near infrared broadband-filter images to analyze the properties of the stellar population. WFPC-2 Hα image and ground-based spectroscopy allow us to study the Balmer emission lines. Finally, *Chandra*/ACIS X-ray images provide resolved distribution of the X-ray emission at various energy bands. The observational data are analyzed by comparison with the predictions from evolutionary synthesis models to constrain the properties of the star formation episode.
Results. The UV, Hα and far infrared luminosities of the Haro 2 nuclear starburst are well reproduced assuming a young stellar population with ages ~3.5–5.0 Myr, affected by differential intestellar extinctions. A significant fraction of the stars are completely obscured in the UV, being identifiable only indirectly by their contribution to the ionization of the gas and to the far infrared emission. The diffuse soft X-ray emission extending over the whole source is attributed to gas heated by the mechanical energy released by the starburst. A compact hard X-ray emission (likely an UltraLuminous X-ray source) has been identified in a star-forming condensation to the southeast. Both compact and diffuse Lyα emission components are observed along the major and minor axes in STIS spectral images. Lyα is spatially decoupled from Balmer lines emission, Balmer decrement and UV continuum. However, the diffuse Lyα component is spatially correlated with the diffuse soft X-ray emission. Moreover, unlike the compact Lyα emission, diffuse Lyα shows luminosities larger than predicted from Hα, assuming case B recombination and considering the dust extinction as derived from Hα/Hβ.
Conclusions. The Lyα emission closely associated to the massive stellar clusters is strongly affected by the properties of the surrounding neutral gas (presence of outflows, dust abundance), leading to even a range of escape fractions at different locations within the same starburst. On the other hand, we propose that the diffuse Lyα emission originates in gas ionized by the hot plasma responsible for the soft X-ray radiation, as suggested by their spatial correlation and by the measured $L(\mathrm{H}\alpha)/L_{0.4-2.4\,\mathrm{keV}}$ ratios. Calibration of Lyα as star formation rate tracer should therefore include both effects (destruction vs. enhancement) to avoid biases in the study of galaxies at cosmological distances.

Key words. galaxies: starburst – galaxies: star formation – galaxies: ISM – ultraviolet: galaxies – cosmology: observations – galaxies: individual: Haro 2

1. Introduction

The spectral energy distribution (SED) of galaxies experiencing intense and relatively short episodes of massive star formation (*starbursts*) is dominated in the UV by the continuum of the young, most massive stars. The ionizing radiation they produce interacts with the surrounding gas to produce nebular emission lines through recombination processes. The mechanical energy released during the evolution of these stars, in the form of stellar winds and supernova explosions, heats the medium, producing X-ray emission and collisionally excited emission lines. While Hα is the most prominent hydrogen nebular line in the optical, simple nebular models predict Lyα to be ~9 times more intense than Hα when considering typical nebular parameters for temperature and electronic density (Osterbrock 1989). Nevertheless, observations over the last decades have shown that the value of the $L(\mathrm{Ly}\alpha)/L(\mathrm{H}\alpha)$ may indeed be very different than expected, and that the presence, intensity, spectral shape and spatial profile of Lyα line do depend on many factors (see Mas-Hesse et al. 2003; Atek et al. 2009; Hayes et al. 2010; Östlin et al. 2009,

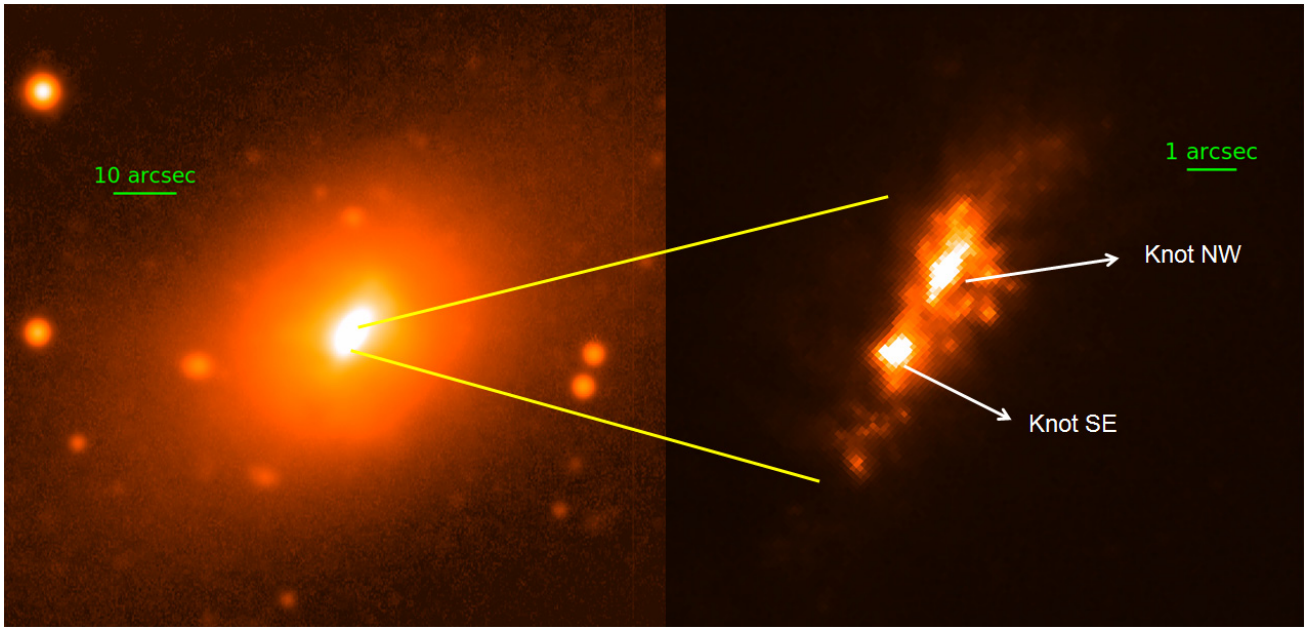

Fig. 1. *Left*: image of the whole galaxy Haro 2 from NOT/ALFOSC in the *V*-band. *Right*: image of the UV-continuum of the nucleus of Haro 2 obtained with HST/WFPC-2 with filter *F336W* where knots SE and NW are labelled.

and references therein). Lyα is a resonant line and this causes Lyα photons to be absorbed and reemited by neutral hydrogen atoms within the gas many times before they can escape. The increase in the path of the photons at Lyα wavelength due to this resonant effect implies that very little dust can completely destroy the photons around 1216 Å, yielding a damped Lyα absorption (Chen & Neufeld 1994; Atek et al. 2009). However, as explained by Mas-Hesse et al. (2003) and Verhamme et al. (2006), when the mechanical energy injected by the starburst into the interstellar medium (ISM) accelerates the surrounding neutral gas, forming an expanding superbubble, only the blue wing of the emission line is scattered. As a result, Lyα emission can escape from the region, but will show a characteristic P Cyg emission-absorption profile. Mas-Hesse et al. (2003) showed different cases in a sample of blue compact galaxies in the Local Universe, ranging from damped absorption to emission with and without P Cyg profiles, depending on the kinematical and ionization properties of the medium surrounding the star-forming regions. Verhamme et al. (2006) computed the different profiles expected applying radiation transfer models to different scenarios, including the presence/absence of accelerated gas, dust, energy shift of the photons by the scattering process, ...

Tenorio-Tagle et al. (1999) proposed a sequence of Lyα profiles following the different evolutionary phases of the starburst, assuming the acceleration of the neutral gas by the ongoing starburst and the formation of expanding shells to be the driver of the Lyα line visibility. Since the acceleration of the surrounding ISM is responsible for both the generation of X-ray emission, by the process of gas heating (Strickland & Stevens 1999), and for the escape of the Lyα emission line, by opening kinematical "holes" in the neutral gas, we expect some intrinsic correlation between both phenomena. In order to study this possible correlation we embarked in a project to study the X-ray properties of Lyα emitters in the Local Universe, starting with Haro 2.

Haro 2, also known as Mrk 33, Arp 233 and UGC 5720, is a metal-rich blue compact dwarf galaxy (Davidge 1989), experiencing an intense star-forming episode with an age of ~5 Myr (Mas-Hesse & Kunth 1999). Star formation is located in the nucleus of the galaxy where it can be resolved into individual knots (Fig. 1). Chandar et al. (2004) combined the HST/STIS spectra of six different clusters within the starbursting nucleus, whereas Méndez & Esteban (2000) could only resolve three knots in an Hα image obtained with the HIRAC camera of the Nordic Optical Telescope. On the other hand, Summers et al. (2001) detected two knots in a *B*-band image from the *Jacobus Kapteyn* Telescope. Besides the young population produced in the current star-formation episode Fanelli et al. (1988) argued for the existence of an older stellar population given the spectral features of A-type stars found by the International Ultraviolet Explorer (IUE). Based on the data by Fanelli et al. (1988), Summers et al. (2001) decomposed the star formation history of Haro 2 into a current starburst of ~5 Myr, a previous burst of ~20 Myr and an earlier episode having ocurred ~500 Myr ago. Despite being a metal rich, rather dusty galaxy, Lequeux et al. (1995) found that Haro 2 is an intense Lyα-emitter. The line shows a clear P Cyg profile apparently originated by a neutral superbubble expanding at ~200 km s^{-1}, energized by the central starburst. Mas-Hesse et al. (2003) obtained a high-resolution spectral image with HST/STIS in the Lyα range along the minor axis, showing the P Cyg profile and the spatial decoupling of the continuum and the Lyα emission. Summers et al. (2001) performed a study of the X-ray radiation of Haro 2 based on ROSAT/HRI data and proved that the mechanical energy released by the nuclear starburst was indeed powering the diffuse, soft X-ray emission. These authors quantified in 2% the fraction of the mechanical energy injected by the burst into the medium ending up being emitted as X-rays. Legrand et al. (1997) identified the large Hα shell at the edges of the expanding superbubble, decoupled from the rotation velocity of the galaxy.

The bolometric luminosity of Haro 2 is well represented by its infrared luminosity $L_{\rm FIR} = 1.4 \times 10^{43}$ erg s^{-1}, which overlaps with the $L_{\rm bol}$ low-end in the luminosity function of Lyman-α emitting galaxies (LAEs) at $z = 3.1$ (Gronwall et al. 2007). Haro 2 also shows an UV continuum luminosity similar to that of the weakest Lyman Break Galaxies (LBGs) in the redshift range $z = 2.7-5$ (Tapken et al. 2007). This fact, together with its high

Table 1. Haro 2 coordinates, distance, scale, Galactic HI, color excess toward the source, and oxygen abundance.

RA (J2000.0)	Dec (J2000.0)	Redshift[a]	Distance[a] (Mpc)	Scale[a] (pc arcsec^{-1})	N(HI)[b] (cm^{-2})	$E(B-V)_{\rm Gal}$	$12+\log({\rm O/H})$[c]
10 32 31.9	+54 24 03.7	0.004769	20.5	100	6.3×10^{19}	0.012	8.5

Notes. [(a)] From NED (the NASA/IPAC Extragalactic Database). [(b)] Value from Lequeux et al. (1995). [(c)] Value from Davidge (1989).

Table 2. Log of HST/FOC, HST/NICMOS, HST/WFPC2 and *Chandra* observations of Haro 2 used in this work.

Instrument	Observation date	Filters	Integration time (s)	λ_0 (Å)	Plate scale (arcsec pixel^{-1})
HST/FOC[(a)]	1993 Apr. 18	*F220W*	1197	2328	0.02
HST/NICMOS	2006 Sep. 28	*F160W*	912	1.6×10^4	0.075
HST/WFPC2	2009 Mar. 9	*F336W*	3300	3332	0.10
HST/WFPC2	2009 Mar. 9	*F658N*	1800	6591	0.10
HST/WFPC2	2009 Mar. 9	*F555W*	600	5304	0.10
HST/WFPC2	2009 Mar. 9	*F814W*	600	8337	0.10
Chandra/ACIS	2008 Feb. 2	–	19 194	–	0.49

Notes. [(a)] Observation performed before COSTAR deployment.

Lyα-intensity and P Cyg spectral profile, makes of Haro 2 a good local prototype of high-z Lyα-emitters whose star formation activity is usually derived from both Lyα luminosity, UV continuum and/or X-ray emission. Understanding the processes determining these emissions in a closeby galaxy which can be studied in high detail is of paramount importance to quantify the star formation activity in distant galaxies. The basic properties of Haro 2 are summarized in Table 1.

In this paper we have analyzed observations obtained by HST with STIS, NICMOS and WFPC-2, and by *Chandra* in X-rays, as well as data obtained from ground-based observatories, to fully characterize the properties of the star formation episodes taking place in the nucleus of Haro 2 and of its associated X-ray and Lyα emissions. In Sect. 2 we describe the HST, *Chandra* and ground-based observations. In Sect. 3 we present the results obtained from the analysis of the observational data, which we discuss later in Sect. 4. Section 5 contains the conclusions of the study.

Throughout this paper we will consider 20.5 Mpc as the distance to Haro 2, which yields a projected scale of $\sim$100 pc arcsec^{-1}. We want nevertheless to remark that the distance to Haro 2 could be larger, when compared to IZw18, whose estimated distance has been increased by a factor of almost 2 to 19.5 Mpc by the analysis of Color Magnitude Diagrams and Cepheid variables. The absolute values concerning luminosities, masses and so on should be taken with a word of caution, although they do not affect our conclusions.

2. Observational data

2.1. HST observations: ultraviolet, optical and near infrared

We have used observations of Haro 2 obtained with STIS, WFPC-2 and NICMOS, in the UV, optical and near infrared ranges, obtained from the HST Archive at STScI. In this section we describe the data and the processing done.

2.1.1. HST images

The HST imaging data sets used are listed in Table 2. There is a single UV image of Haro 2, obtained with FOC in 1993, before COSTAR was installed. The observation was performed with the *F220W* filter. The far-UV image covers $\sim21'' \times 23''$ with plate scale of $\sim0.02''$ pixel^{-1}, and is centered on $\lambda = 2328$ Å. The FOC image is shown in Fig. 2, together with the STIS slits directions perpendicular to the major axis (direction D1) and parallel to it (direction D2). Since UV emission is dominated in star-forming regions by massive stars, with this FOC image we can study the UV-morphology of the starburts located in the nucleus of the galaxy, as well as calculate the UV-flux at $\lambda = 2328$ Å ($F_{\rm UV}$, hereinafter) emitted by each knot and by the total source as a whole. To derive the $F_{\rm UV}$ flux of each knot we defined two similar and non-overlapping boxes, as indicated in Fig. 2. The boundaries of these boxes are rather arbitrary, since we can not discriminate beween both components, but the flux inside them should be dominated by the bright stellar clusters within knots NW and SE. The sizes of the boxes are $7.4'' \times 5.5''$ (knot NW) and $7.4'' \times 4.8''$ (knot SE). We have checked that the brightest knots account indeed for 70–80% of the total UV flux measured on each box, dominating so their integrated spectral properties. As we will discuss later, while the properties of the starburst will be therefore dominated by the massive stars in the bright knots, we have used the total flux within the boxes to derive the mass normalization when applying evolutionary synthesis models.

Background on the FOC image was estimated from the most separated regions away from the source, averaging on boxes of 3×3, 5×5 and 10×10 pixel^2. The UV-background was estimated to be $\sim$0.75 counts pixel^{-1}. In order to work with an image free from background contamination, we subtracted this average background from all pixels of the image. After that, the intensity was multiplied by `PHOTFLAM` and divided by the total exposure time `EXPTIME` in order to work with fluxes in units of erg s^{-1} cm^{-2} Å^{-1}.

We studied the effect of FOC point spread function (PSF) since the image was obtained prior to COSTAR deployment. We downloaded a pre-COSTAR PSF for an F/96 *F220W* observation performed five months earlier from the instrument website[1] and extracted the enclosed point source flux within the boundaries of the boxes we have considered. It was found that for the sizes

[1] http://www.stsci.edu/hst/foc/calibration/f96_nov1992.html

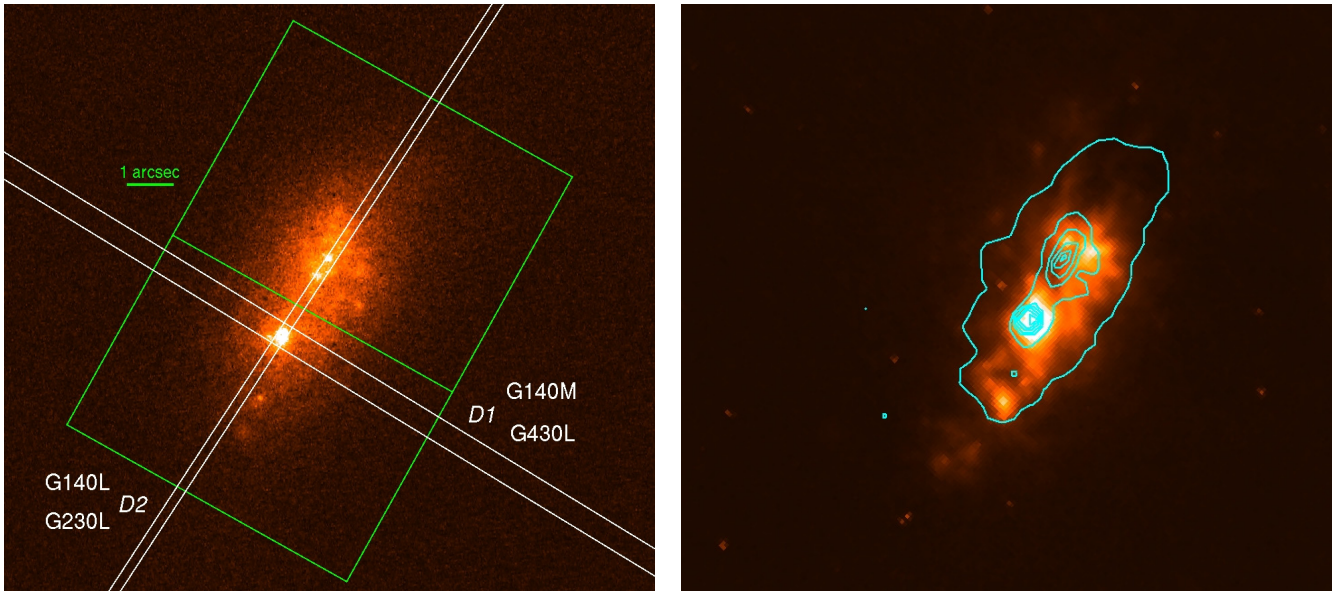

Fig. 2. *Left*: ultraviolet HST/FOC image of Haro 2, together with the locations of the HST/STIS slits D1 (gratings G140M and G430L) (Mas-Hesse et al. 2003), and D2 (G140L and G230L) (Chandar et al. 2004), and the boxes used to extract the UV flux from each knot. The width of the slits is represented at real scale. North is up and east is left. *Right*: Hα image obtained with HST/WFPC2, with the UV continuum contours superimposed.

and locations of the regions considered and assuming the knots are point-like sources, a ∼85% of the total radiation is included within the integration area, hence leading to an underestimation in the total $F_{\rm UV}$ of less than ∼15%.

Haro 2 has been observed with HST/WFPC2 in the UV-optical range with broad-band filters *F336W*, *F439W*, *F555W* and *F814W*, providing images of the continuum emission, and with the narrow filter *F658N*, which is dominated by Hα. In order to isolate the Hα-emitting regions, continuum was subtracted from the *F658N* image using the *F814W* one, assuming it represents well the continuum at Hα. After downloading the data from the HST archive, drizzled files were combined and aligned for filters *F814W* and *F658N*. Then, the resulting images were multiplied by `PHOTFLAM` in order to convert counts into flux values. Finally, the *F814W* image was multiplied by an arbitrary constant and then subtracted from the *F658N* image, using field stars as reference.

Finally, we downloaded from HST archive an image of Haro 2 obtained by NICMOS at 1.60, μm with broad-band filter *F160W*. Its size is 19.2″ × 19.2″, and the scale of the pixel is 0.075″. No background subtraction on the science data file was necessary since NICMOS reduction pipeline already performs this removal through task `cnib`. The NICMOS *F160W*, WFPC-2 *F336W* and WFPC-2 Hα images have been color-coded and combined in Fig. 3.

The astrometry included in the World Coordinate System (WCS) keywords in the headers of the different images was not always consistent, with relative offsets of up to ∼1.2″ between the NICMOS and FOC images, for example. We have taken the HST/NICMOS header information as reference, which matched well the *Chandra* one, and have corrected the astrometry from other images when needed.

2.1.2. HST spectroscopy

Mas-Hesse et al. (2003) studied spectral images obtained with the G140M and G430L grating on STIS, with a 52″ × 0.5″ long slit placed orthogonal to the major axis of the nucleus. This high resolution spectral images covered the range 1200–1250 Å, including the Lyα line, and 2900–5700 Å, comprising the oxygen lines O[II]3727 and O[III]4959, 5007, and Hβ. Although the integration time on this optical spectral image was very short, it provides the spatial profiles of these lines with high angular resolution. Hereinafter, we will refer to the direction of this slit as D1. Furthermore, Chandar et al. (2004) analyzed two additional spectral images using the G140L and G230L gratings with the 52″ × 0.2″ long slit oriented along the major axis of the star-bursting region. These spectral images cover the spectral ranges 1150–1730 Å, showing the Lyα emission and the stellar absorption lines Si IV1394, 1403 and C IV1548, 1551, and 1570–3180 Å. This direction will be referred to as D2. Information on both UV-optical observations is listed in Table 3, and in Fig. 2 both slit directions can be observed superimposed on the FOC image. Both slit directions are orthogonal, and whereas Mas-Hesse et al. (2003) encloses only the SE star-forming knot, slit from Chandar et al. (2004) contains the bulk emission from both SE and NW knots. The G140M D1 and G140L D2 spectral images constitute the direct observation of the Lyα morphology and spectroscopy of Haro 2 which we analyze in this work.

Extraction, background removal and analysis of the STIS D1 data were already discussed in detail by Mas-Hesse et al. (2003). Data were reduced with STSDAS procedures and flux from 100 rows above and below the stellar continuum were averaged to estimate the geocoronal Lyα emission and the detector background, being the latter negligible. Slit correction was performed by multipliying measured counts by the STIS parameter `diff2pt`. Observational data for filters G140L and G230L in D2 were downloaded from the HST archive already calibrated. Again, intensity values measured were multiplied by `diff2pt` in order to correct for slit losses. After that, the first step was to select the continuum regions, deriving continuum extensions within the slit of ∼60 pc and ∼150 pc for both knots SE and NW respectively (see Table 6). The integration of the contributions from each of the regions of the spectral images, and the merging of the observations performed with each grating were done with IRAF-STSDAS procedures.

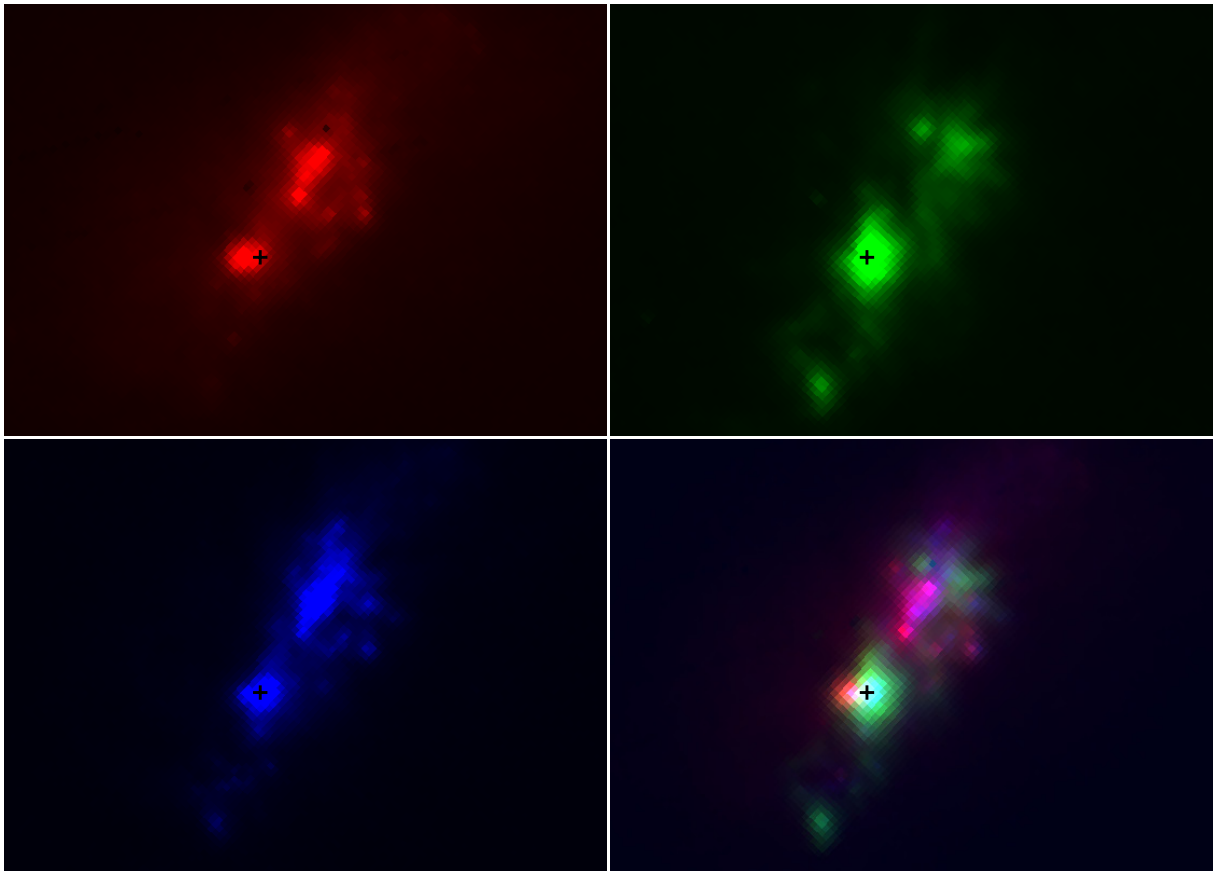

Fig. 3. Multiwavelength images of Haro 2: NICMOS *F160W* near-infrared continuum (red), WFPC-2 *F336W* UV continuum (blue) and Hα emission (green). Images are 10 arcsec wide. The black cross marks the center of the bluest stellar cluster in knot SE. Note the red stellar population to the east of knot SE, and disperse within knot NW. North is up and east is left.

Table 3. Log of HST/STIS observations of Haro 2 used in this work.

Observation date	Grating	Integration time (s)	Position angle (deg)	Slit direction	Slit size	Wavelength interval (Å)	Plate scale (arcsec pixel^{-1})	Spectral dispersion (Å pixel^{-1})
2000 Dec. 1	G140M	7900	−121.35	D1	$52'' \times 0.5''$	1200–1250	0.029	0.053
2000 Dec. 1	G430L	300	−121.35	D1	$52'' \times 0.5''$	2900–5700	0.050	2.746
2003 Feb. 26	G140L	1446	146.85	D2	$52'' \times 0.2''$	1150–1730	0.025	0.584
2003 Feb. 26	G230L	600	146.85	D2	$52'' \times 0.2''$	1570–3180	0.025	1.548

We noticed that keywords `RA_APER` and `DEC_APER` in the headers of the G140M and G430L HST/STIS file did not correspond to the actual position of the slit, centered on knot SE, but rather referred to an intermediate position closer to knot NW. From the Hα image obtained with HST/WFPC-2 data we extracted two different spatial profiles, one assuming the position of the slit indicated by the HST/STIS observation file and which is centered close to knot NW, and another profile for a slit placed on knot SE. The angle of the slit was fixed to the value indicated in the file header. Given the same nature of Balmer lines Hα and Hβ, we compared the extracted Hα profiles with the Hβ profile from HST/STIS G430L observation, and they only agree when the slit is assumed to be centered on knot SE. We did the same comparison between profiles extracted from the HST/WFPC-2 *F555W* image and the profile of the composite Hβ+O[III]4959, 5007+*continuum* obtained from the HST/STIS G430L observation and the match is only possible when the slit is placed on knot SE. Therefore, we concluded that HST/STIS G140M and G430L observations of Haro 2 are centered on knot SE and in Fig. 2 this slit is located accordingly.

2.2. Chandra: X-rays

Chandra time was allocated under proposal 09610593 (PI: J. Miguel Mas-Hesse) to observe Haro 2 with ACIS. Observation 9519 with time duration of ∼20 ks (see Table 2) was performed on February 2, 2008. *Chandra*/ACIS data were reduced with CIAO 4.1 following the standard reduction procedures available on the *Chandra*-CIAO website, reprocessing level 1 and 2 event files. The Ancillary Response File (ARF) and the redistribution matrix file (RMF) were also calculated. In order to obtain the X-ray spectrum of Haro 2 source counts were extracted from a circular region of radius ∼9″ centered on the bulge emisison since it incloses most of the X-ray radiation of the source. This region is shown in Fig. 4 labeled as NUCLEUS. Background was extracted from a composite of three circular regions with radius ∼46″, 56″, 58″ from the area surrounding the galaxy and not containing any other bright source. A net total count rate of $\sim 1.4 \times 10^{-2}$ cts s^{-1} after background subtraction was measured for the whole energy range in NUCLEUS. Spectral analysis was performed with XSPEC v.12.7 (Arnaud 1996), grouping source

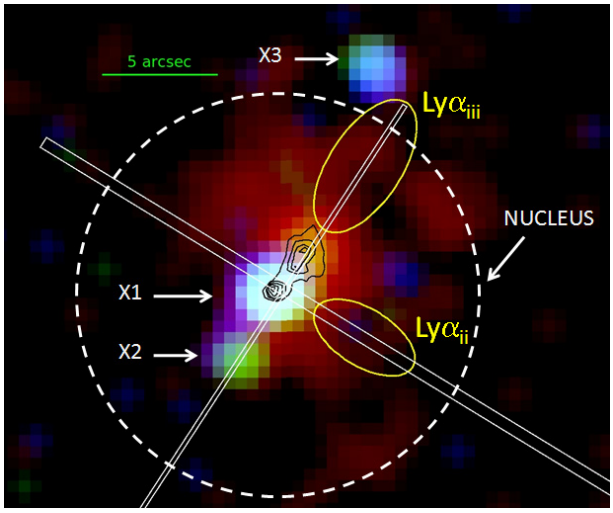

Fig. 4. Color-coded *Chandra* X-ray image of Haro 2: soft (0.2–1.5 keV, red), medium (1.5–2.5 keV, green) and hard X-rays (2.5–8.0 keV, blue). The contours of the NICMOS near-infrared continuum and the position of the STIS slits have been superimposed. Main X-ray components are labeled. Source region from which X-ray spectrum was extracted is confined within the dashed circle. Regions within the yellow ellipses show diffuse Lyα emission.

counts to have at least 15 counts per bin in order to be able to apply χ^2 statistics in the fitting analysis. The final binned X-ray spectrum of Haro 2 is shown in Fig. 8.

Chandra/ACIS X-ray image is displayed in Fig. 4 color-coded as a function of the energy, where red: 0.2–1.5 keV, green: 1.5–2.5 keV and blue: 2.5–8.0 keV. Color-coded X-ray image is also shown in Fig. 5 with higher detail, together with the composite multiwavelength image at the same scale for reference. We have also superimposed the NICMOS near-infrared contours to identify the positions of the star-forming knots. Haro 2 shows a diffuse soft X-ray emission extended mostly to the N and W of the starbursts, over a region with radius ~600 pc. Also, three hard, point-like sources are observed in Fig. 4 and labeled as X1, X2 and X3. Background-corrected count rates of these hard sources for several energy bands are shown in Table 5, together with the values for NUCLEUS, which includes X1 and X2. X1 is located at the position of knot SE, and is associated to its massive stellar cluster, as we will discuss later. X2 is a source 5 times weaker in the 1.5–8.0 keV band than X1, located to the southeast of knot SE. X2 does not have any correlation to any continuum or Hα emitting region, since, as Fig. 5 shows, the closer UV-optical bright knot is ~1.5″ far. An extra hard object X3 detached from the starburst region is found ~10″ northwest from the nucleus, with a net flux of $\sim 1.5 \times 10^{-3}$ cts s^{-1}. The spectral image obtained with NOT/ISIS in direction D2 (see Sect. 2.3) indicates that the ratio O[II]3727/Hβ in the region close to X3 is two orders of magnitude higher than in the nuclear region. This fact points toward X3 being a source within Haro 2 rather than a background source. However, given its angular distance from the bulk of the X-ray emission and its low flux, we did not analyze it in this work. Therefore, X1 is the dominant component of the hard emission in the NUCLEUS.

2.3. Ground-based observations

An image of Haro 2 obtained with instrument ALFOSC on the Nordic Optical Telescope with filter V_Bes 530_80 is displayed in Fig. 1 (courtesy of Luz Marina Cairós and Ricardo Amorín). Also, two long-slit observations with ISIS on the *William Herschel* Telescope (WHT) were downloaded from the archive for which information is included in Table 4. ISIS spectral images of the source were acquired with slit aligned along directions D1 (red and blue arm in December 25, 2006) and D2 (blue arm in February 9, 2002). Although the observation along D2 was performed only with the blue arm of the instrument, a similar spectral range than the one achieved for direction D1 with both arms was obtained using an observational mode with lower spectral dispersion. As a result, spatial configuration of stellar continuum and main nebular emission lines was obtained along both the major and minor axes of Haro 2. Specifically, we derived from these images the spatial profiles of the Hβ and Hα emission lines.

3. Analysis and results

3.1. HST morphology and photometry

The UV image of Haro 2 nucleus with the identification of its brightest star-forming knots is shown in Fig. 1, together with an image of the whole galaxy in the V-band. The elliptically-shaped nucleus of Haro 2 hosts various massive clusters, located on knots SE and NW. Méndez & Esteban (2000) proposed to differentiate 2 smaller knots within NW, as indeed suggested by Fig. 2. Moreover, Chandar et al. (2004) argued they could identify 6 faint clusters within the galaxy, from the inspection of the UV spatial profile along slit D2 (see Fig. 7). However, for the purposes of this work we will consider only knots NW and SE as individual star-forming regions. These knots are aligned along the major axis, being separated by ~75–100 pc. While knot SE is not resolved, knot NW is more extended and shows a more complex morphology. UV continuum extends few hundreds of parsec away from the knots, so that the whole nuclear star-forming region has a size of $\sim 750 \times 1000$ pc^2.

The UV-flux values for each knot and for the whole starburst region were extracted from the FOC image considering boxes shown in Fig. 2 with sizes 7.4″ × 5.5″ for knot NW and 7.4″ × 4.8″ for knot SE. As explained above, due to the proximity between knots NW and SE the origin of the counts could not be discerned unambiguously, hence the total flux of the whole source should be taken as a more reliable measure. $F_{\rm UV}$ values for each knot together with their sizes are included in Table 6. The total observed UV emission of the whole galaxy nucleus detected by FOC is $F_{\rm UV} = 2.7 \times 10^{-14}$ erg s^{-1} cm^{-2} Å^{-1} which agrees with the value from the spectrum taken by IUE with a total aperture of 10″ × 20″, which should enclose the whole UV-emitting region. As it will be explained later, masses of the bursts were calculated through the UV flux of each of the knots using evolutionary population synthesis models.

Comparison of NICMOS image of IR continuum at 1.60 μm with the WFPC-2 image of the UV continuum at 3300 Å (see Fig. 3) shows that some regions which are very prominent in the IR are not visible in the UV. This results especially evident on knot SE, as well as in some more diffuse areas of knot NW. Since both knots are dominated by young, massive stars, the non-detection in the UV of the stars detected in the IR is probably due to a patchy distribution of dust, which hides part of the young population, or to evolutionary effects on different populations.

The Hα image obtained with HST/WFPC2 is shown in Fig. 2 (right), with the UV continuum contours superimposed. The

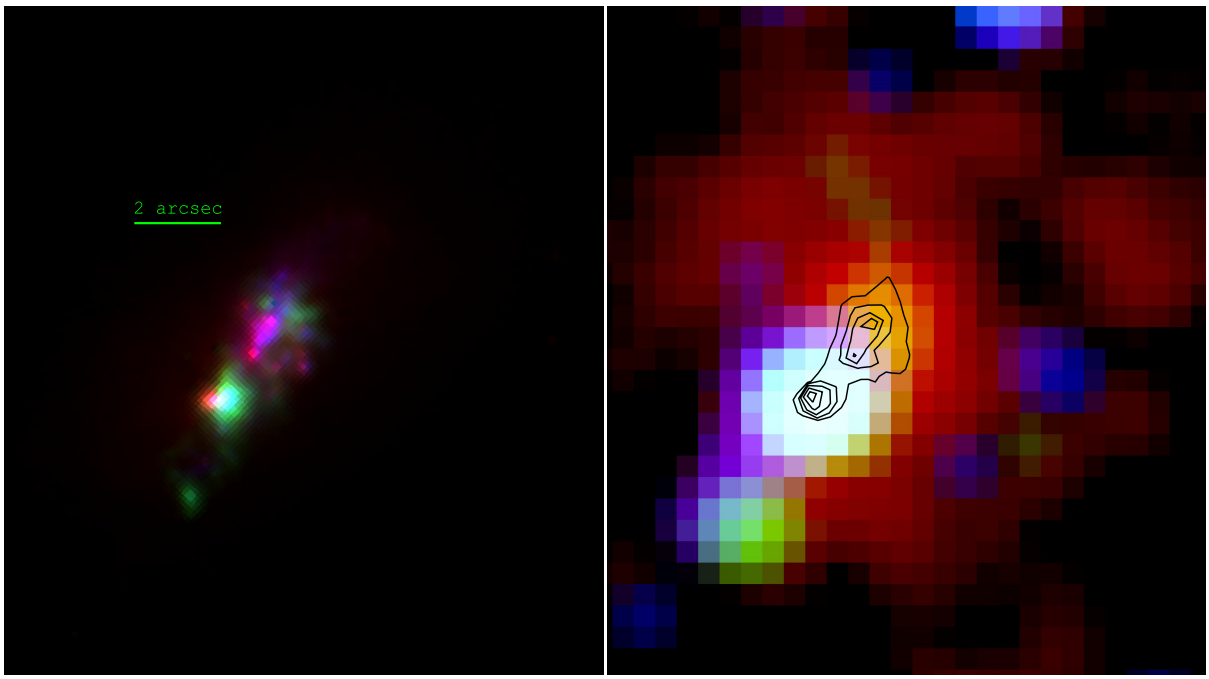

Fig. 5. *Left*: multiwavelength image of Haro 2, as in Fig. 3. *Right*: the color-coded *Chandra*/ACIS X-ray image (colors as in Fig. 4) at the same scale, with the NICMOS contours superimposed for reference. North is up and east is left.

Table 4. Log of WHT/ISIS observations of Haro 2 used in this work.

Observation date	Arm	Grating	Integration time (s)	Position angle (deg)	Slit direction	Slit size	Wavelength interval (Å)	Plate scale (arcsec pixel^{-1})	Spectral dispersion (Å pixel^{-1})
2006 Dec. 25	Blue arm	R600B	3600	−121.35	D1	$3.3' \times 1.0''$	3460–5280	0.20	0.45
2006 Dec. 25	Red arm	R600R	3600	−121.35	D1	$3.3' \times 1.0''$	5690–7745	0.22	0.49
2002 Feb. 9	Blue arm	R300B	3600	146.85	D2	$4.0' \times 1.1''$	3480–7020	0.20	0.86

Table 5. Count rates of X-ray objects corrected for background contamination.

Object	Total (s^{-1})	Soft (0.2–1.5 keV) (s^{-1})	Medium (1.5–2.5 keV) + Hard (2.5–8.0 keV) (s^{-1})
NUCLEUS	2.0×10^{-2}	1.2×10^{-2}	3.2×10^{-3}
X1	6.8×10^{-3}	4.2×10^{-3}	2.1×10^{-3}
X2	8.9×10^{-4}	3.6×10^{-4}	4.2×10^{-4}
X3	1.5×10^{-3}	4.2×10^{-4}	6.3×10^{-4}

Hα emission appears associated and essentially co-spatial to both stellar clusters SE and NW.

3.2. UV continuum

High spectral resolution UV spectra are available in Starburst99 models (Leitherer et al. (1999), hereinafter SB99 models) in the range 1200–1600 Å for the LMC/SMC library and 1200–1800 Å for the Milky Way library, with a spectral step of 0.75 Å. Normalized spectra for both knots in the wavelength range 1150–1700 Å were extracted from STIS spectral image obtained in the direction D2 with filter G140L. The spatial extension of the stellar continuum regions considered was 0.6″ and 1.5″ for knots SE and NW, respectively. Given the sentivity of the shape and intensity of the absorption lines Si IV1394, 1403 and C IV1548, 1551 to the age of the burst, normalized UV spectra from both knots were fitted individually with SB99 UV models in order to calculate their evolutionary state. SB99 models were computed for an initial mass function $\phi(m) \sim m^{-2.35}$ (i.e. a Salpeter IMF) and mass limits of 2–120 $M_\odot$, assuming instantaneous star formation and $Z = 0.008$ for the evolutionary tracks and high-resolution spectra. This metallicity is the closest available to the observational one $Z \sim Z_\odot/2$ (Davidge 1989). UV line spectra from the models were either taken from the Milky Way or the LMC/SMC libraries. We found that no acceptable fitting of the normalized spectrum of either knot was possible with the LMC/SMC library whereas a good agreement was reached when the Milky Way library was used. We obtained ages of ∼4 Myr and ∼5 Myr for knots SE and NW. Uncertainties in the procedure may yield a precision in the values of the ages obtained of approximately ±0.5 Myr. The final fittings of the normalized spectra are shown in Fig. 6.

Reddening in Haro 2 was calculated through the fitting of the UV SED of each knot with the SB99 models, given the assumptions for IMF and metallicity already explained above. SEDs of the models at the ages 4 Myr (for knot SE) and 5 Myr (for knot NW) were reddened for a certain value of the color

Table 6. Physical properties of knots NW and SE in Haro 2, assuming a single stellar population at each knot, with mass normalization according to their integrated UV luminosity (see text for details).

Knot	Age (Myr)	Mass ($M_\odot$)	$E(B-V)^a$	$F_{\rm UV}$ (erg s^{-1} cm^{-2} Å^{-1})	$L_{\rm UV}{}^b$ (erg s^{-1} Å^{-1})	Stellar extension^c (pc)
Knot SE	~4	7.0×10^5	0.050	1.1×10^{-14}	5.5×10^{38}	~60
Knot NW	~5	1.3×10^6	0.020	1.7×10^{-14}	8.5×10^{38}	~150

Notes. $^{(a)}$ Internal color excess assuming Prévot et al. (1984) extinction law (SMC). $^{(b)}$ Luminosity value not corrected for Galactic or intrinsic extinctions. $^{(c)}$ Extension of the stellar continuum along direction D2 in the STIS spectral image.

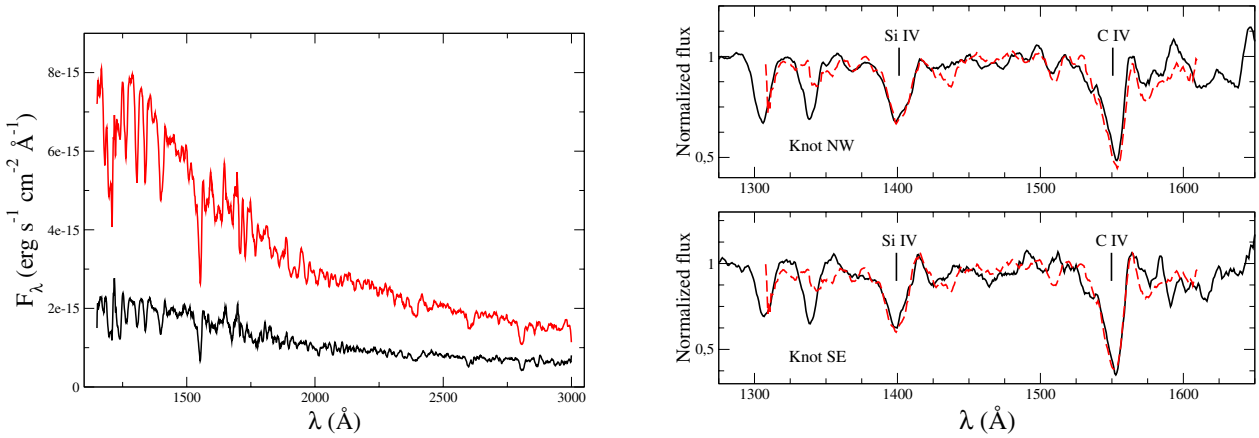

Fig. 6. *Left*: observed UV stellar continuum of knot SE (bottom) and knot NW (top). *Right*: normalized spectrum of UV stellar continuum of knots SE and NW (solid lines) with absorption lines Si IV1394, 1403 and C IV1548, 1551 fitted with SB99 models for ages ~4 Myr and ~5 Myr (dashed lines), respectively (see text for details).

excess $E(B-V)$ and assuming SMC extinction law (Prévot et al. 1984) and $R_V = 3.1$, then they were redshifted and finally extinguished for Galactic extinction for the color excess $E(B-V) = 0.012$ assuming Cardelli extinction law (Cardelli et al. 1989). Redshift was obtained from the Gaussian fit of the Hβ line included in the spectrum of the G430L observation, which turned out to be $z = 0.00461$, that is within ~4% the value reported in NED (NASA/IPAC Extragalactic Database). Iterative method for calculating $E(B-V)$ was repeated until a good fit was achieved for each knot, obtaining $E(B-V)_{\rm knot\,SE} \sim 0.050$ and $E(B-V)_{\rm knot\,NW} \sim 0.020$. Observed spectra are shown in Fig. 6. Finally, the masses of both knots were calculated dividing the observed UV luminosity $L_{\rm UV}$ of each knot measured by HST/FOC by the reddened, redshifted, predicted value from the SB99 models, which is computed per unit mass, obtaining $M_{\rm knot\,SE} \sim 7 \times 10^5\ M_\odot$ and $M_{\rm knot\,NW} \sim 1.3 \times 10^6\ M_\odot$. These values are obtained when considering IMF mass limits of 2–120 $M_\odot$. Were other boundaries of the mass range be considered, a proper correction should be performed to these values (Wilkins et al. 2008; Otí-Floranes & Mas-Hesse 2010). Given the difficulties to discern the actual flux of each knot from the total one, the values of the masses calculated should be taken as a rough estimate. As explained in Sect. 2.1.1, this procedure assumes that the stars contributing to the diffuse UV continuum within each box, as indicated in Fig. 2, share the same age as those in the central knots dominating the UV spectral features. While this should be considered just as a first order approximation, this strategy provides a more realistic global mass normalization than just considering the flux within the unresolved knots. A correct normalization is required to properly compare the predictions with globally integrated magnitudes, such as the X-ray or far infrared luminosities.

Physical properties calculated through evolutionary population synthesis models for knots SE and NW are shown in Table 6. Given the small volume of knot SE, which we can not resolve, and its mass, $M_{\rm knot\,SE} > 1 \times 10^5\ M_\odot$, this knot should be considered a super stellar cluster (Adamo et al. 2010).

We want to stress that the results of the fit discussed above are based on the UV continuum and spectral features as observed with STIS. $L_{\rm FIR}$ and L(Hα) emissions provide us with a consistency check to verify the validity of the fitting. Once the parameters of the models were calculated, we compared their predictions of $L_{\rm FIR}$ and L(Hα) with the observational values. Observed $L_{\rm FIR}$ luminosity was calculated through the relation of Helou et al. (1985) given the IRAS fluxes $F_{60\,\mu{\rm m}} = 4.7$ Jy and $F_{100\,\mu{\rm m}} = 5.3$ Jy. Since this relation yields the infrared emission collected in the wavelength range 42.5–122.5 μm, it should be corrected in order to obtain the total emission in the complete infrared range. As was found by Calzetti et al. (2000) for a sample of eight starburst galaxies, the ratio FIR(1−1000 μm)/FIR(40−120 μm) ~ 1.75, hence the value obtained from Helou et al. (1985) relation was multiplied by 1.75, yielding $L_{\rm FIR} = 2.0 \times 10^{43}$ erg s^{-1}. On the other hand, Moustakas & Kennicutt (2006) measured the integrated intensities and the equivalent widths of the Balmer and forbidden lines for more than 400 galaxies using drizzled spectroscopic observations with Boller & Chivens spectrograph on Bok telescope. Intensities and equivalent widths of all lines were corrected for Galactic reddening and stellar absorption, and also for [NII] contamination in the case of Hα, obtaining for Haro 2 $F(\text{H}\alpha) = 1.6 \times 10^{-12}$ erg s^{-1} cm^{-2}. Since their extraction aperture was of 50″ and the slit was drifted along 40″, this value is expected to represent well the total flux associated to the burst. The same F(Hα) value for Haro 2 was measured by Gil de Paz et al. (2003). Moreover, besides the integrated values,

Table 7. Predicted values of the ages, masses, stellar and nebular extinctions and emissions of Populations 1, 2 and the composite of both, as well as the $EW(\mathrm{H}\beta)$ produced. Observational values are also displayed.

Population	*Age* (Myr)	M ($M_\odot$)	$E(B-V)_*$	$E(B-V)_{\rm neb}$	$L_{\rm UV}{}^a$ (erg s^{-1} Å^{-1})	$L(\mathrm{H}\alpha)^a$ (erg s^{-1})	$L_{\rm FIR}$ (erg s^{-1})	$EW(\mathrm{H}\beta)$ (Å)
1	4.5	1.8×10^6	0.035	0.24	1.3×10^{39}	2.5×10^{40}	3.4×10^{42}	–
2	3.5	2.0×10^6	0.5	0.24	7.1×10^{37}	5.3×10^{40}	1.6×10^{43}	–
1+2	–	3.8×10^6	–	0.24	1.4×10^{39}	7.8×10^{40}	2.0×10^{43}	58
Observed	–	–	–	0.24[b]	1.4×10^{39}	7.8×10^{40}[b]	2.0×10^{43}	44–80[b]

Notes. [(a)] Luminosity value reddened by Galactic and intrinsic extinctions. [(b)] Value from Moustakas & Kennicutt (2006).

Moustakas & Kennicutt (2006) reported the values of nuclear regions using an aperture of 2.5″ × 2.5″. Nebular reddening calculated through the ratios of the integrated Balmer lines values from Moustakas & Kennicutt (2006) is $E(B-V)=0.24$, which is in perfect agreement with the value $E(B-V)=0.22$ reported by Mas-Hesse & Kunth (1999). This value is ∼0.2 dex larger than the values found by continuum SED fitting for knots SE and NW. Higher extinction for nebular gas than for stellar continuum has been observed in several star-forming regions (see Maíz-Apellániz et al. 1998; Calzetti et al. 2000). This disagreement is usually attributed to the fact that young clusters clean its surroundings from dust, leaving relatively clear holes through which the UV continuum escapes with low attenuation. On the other hand, the more extended ionized gas still contains a significant amount of dust.

$L_{\rm FIR}$ and $L(\mathrm{H}\alpha)$ were calculated with the evolutionary synthesis models by (Cerviño et al. 2002; hereinafter CMHK02 models). $L_{\rm FIR}$ is produced by the emission of dust, which is assumed to be in thermal equilibrium. The models compute the energy absorbed by dust, comparing the intrinsic UV-optical continuum with the observed one, and assumes that all the missing energy is reemitted as $L_{\rm FIR}$. In addition, the models assume that a fraction $1-f=0.3$ of the ionizing photons is directly absorbed by dust and does not contribute to the ionization. $L_{\rm FIR}$ and $L(\mathrm{H}\alpha)$ were estimated with the CMHK02 models for the knots SE and NW, assuming the values (mass, age, reddening, ...) obtained in the previous analysis and shown in Table 6. When the values of $L_{\rm FIR}$ and $L(\mathrm{H}\alpha)$ were compared to the observational ones we found that the models severely underestimated both the $L_{\rm FIR}$ and $L(\mathrm{H}\alpha)$ luminosities by factors 7 and 3, respectively.

This disagreement points to the existence of an extremely reddened stellar population, whose contribution to the UV continuum is negligible in the FOC image and the STIS spectra, but which contributes significantly to both the observed FIR and Hα emissions. Moreover, the high underestimation of $L(\mathrm{H}\alpha)$ points to a young population, with a relatively strong ionizing power. Therefore, in order to explain all observables we built a simplified model based on the existence of two populations: Population 1, which appears as a conspicuous UV-emitter, and Population 2, which is highly reddened and is the main contributor to $L_{\rm FIR}$ and $L(\mathrm{H}\alpha)$. We defined three equations with the observables UV, FIR and Hα fluxes being the sum of the reddened contributions by each of the populations, where their masses M_1 and M_2 and the stellar extinction of Population 2 $E(B-V)_{*,2}$ are the unknowns. The contribution by each population was calculated with the CMHK02 models assuming the corresponding parameter values. A mean age of $Age(1)=4.5$ Myr and stellar reddening $E(B-V)_{*,1}=0.035$ were assumed for Population 1, combining the results for both knots NW and SE and mean nebular extinction was assumed to be $E(B-V)_{neb}=0.24$ (Mas-Hesse & Kunth 1999; Moustakas & Kennicutt 2006) irrespective of the population. For each age of Population 2 considered ($Age(2)$), a system of three equations with three unkowns was obtained and solved. The results show that in order to reproduce the observed values, stars from Population 2 must be in a less evolved state than those of Population 1, which agrees with the former being more reddened having had less time to clean the surroundings. Values $Age(2)=3.5$ Myr and stellar color excess $E(B-V)_{*,2}=0.5$ can account for the total UV, Hα and $L_{\rm FIR}$ emissions. Assuming lower values for $E(B-V)_{*,2}$ implies a higher contribution by Population 2 to the UV emission, which as we have discussed is ruled out by the FOC image and the STIS spectrum. Values found for M_1, M_2 and $E(B-V)_{*,1-2}$ are included in Table 7 together with the ages considered, the contribution by each population to the magnitudes observed and the global $EW(\mathrm{H}\beta)$. Values from Table 6 do differ from those of Population 1 of Table 7 since different assumptions were made in each case. The values given in Table 6 correspond to the average properties of the subsample of massive stars which are less affected by interestellar extinction, while a similar fraction of young stars seems to be still too obscured to be detected in the UV. While this is a simplified scenario, it shows that in reality the knots of Haro 2 are probably formed by young massive stars with an age within ∼3.5–5 Myr, and a continuous sequence of interstellar extinction, spanning from regions almost devoid of dust to others mostly blocked in the UV by dense dust clouds.

The underestimation of the Balmer and FIR emissions in Haro 2 when assuming a starburst mass derived from the UV flux was also found by Mas-Hesse & Kunth (1999) who, assuming a single reddened stellar population, obtained lower $L(\mathrm{H}\beta)$ and $L_{\rm FIR}$ values than observed by factors 2.3 and 2. These factors differ from ours since Mas-Hesse & Kunth (1999) considered a steeper IMF with slope $\alpha=-3$. On the contrary, they obtained an age for the whole nuclear star-forming region of 4.8 Myr using $EW(\mathrm{H}\beta)$ corrected for both reddening and underlying stellar absorption, which agrees with our estimated value. Using an updated set of models Cerviño et al. (2002) found a value of 4.2 Myr assuming the very same value of $EW(\mathrm{H}\beta)$ from Mas-Hesse & Kunth (1999). Chandar et al. (2004) fitted the UV spectrum from G140L observation along direction D2 using SB99 models and giving different weights to continuum, interstellar lines and stellar wind lines, obtaining the best fit for an age of 5 ± 1 Myr. In all these cases the study was performed over the whole galaxy. Moreover, Moustakas & Kennicutt (2006) obtained $EW(\mathrm{H}\beta)=44$ Å and $EW(\mathrm{H}\beta)=80$ Å for the whole galaxy and the nuclear region, respectively. Both values are already corrected for the Galactic and internal extinctions and stellar absorption. Our prediction from the models when assuming the existence of Populations 1 and 2 of $EW(\mathrm{H}\beta)\sim58$ Å lies between both values.

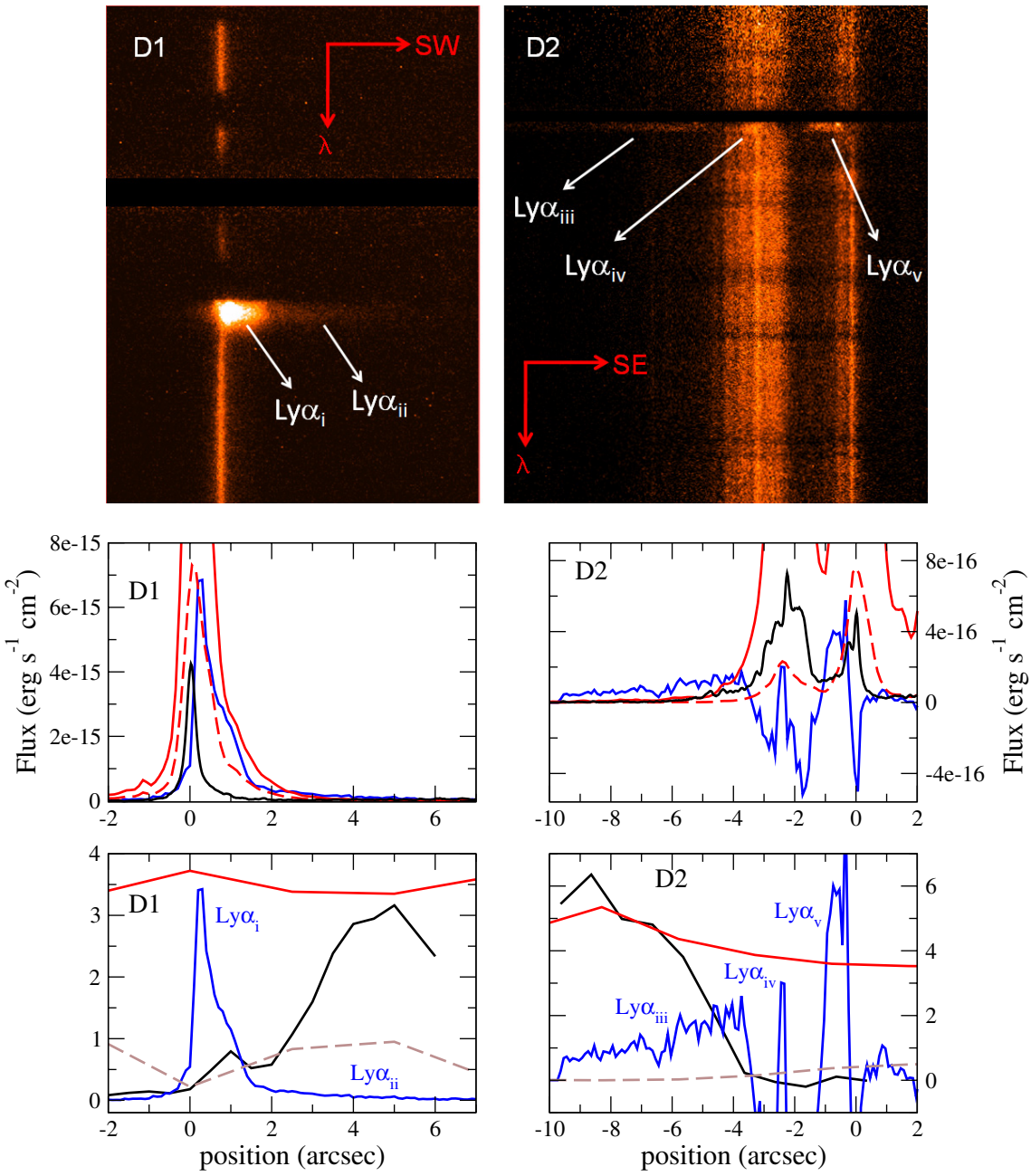

Fig. 7. *Left*: slit along direction D1. *Top-left*: HST/STIS G140M spectral image of Haro 2. *Middle-left*: emission profiles of Lyα (blue) and UV continuum (1175 Å rest frame, black) from STIS data, and Hα (red) from WFPC2 data. *Bottom-left*: spatial profiles of Lyα (blue) and observed Lyα/Hα (black) and Hα/Hβ (from WHT/ISIS data, in red). *Right*: slit along direction D2. *Top-right*: HST/STIS G140L spectral image. *Middle-right*: emission profiles of Lyα (blue) and UV continuum (1227 Å, black) from STIS data, and Hα (red) from WFPC2 data. *Bottom-right*: spatial profiles of Lyα (blue) and observed Lyα/Hα (black) and Hα/Hβ (from WHT/ISIS data, in red). The geocoronal Lyα line has been blackened in both spectral images at the top. In the *middle and bottom panels* positive x-axis corresponds to southwest (*left*) and southeast (*right*). Vertical scale in the *middle panels* corresponds to the Lyα and Hα fluxes. To ease the comparison, the dashed line shows the Hα profile scaled by a factor 0.4 (*left*) and 0.085 (*right*). The vertical scale in the *bottom panels* corresponds to the Lyα/Hα and Hα/Hβ ratios. The brown dashed lines represent the expected Lyα/Hα ratio, assuming case B recombination and applying the internal reddening derived from the observed Hα/Hβ ratio (Balmer decrement), as well as the Galactic extinction.

3.3. Lyα emission

Spectral images on the ultraviolet along the minor (D1 direction) and major (D2 direction) axes in the Lyα wavelength range are displayed in Fig. 7 and a relatively strong Lyα emission is observed in both cases, extending well beyond the stellar clusters. In the case of the observation of knot SE along D1 direction the Lyα-emitting region extends largely to the southwest direction whereas it is much weaker northeast of the stellar cluster. Mas-Hesse et al. (2003) showed that the spatial extension of this Lyα emission along this direction is much larger than the continuum-emitting region. Even more, as observed in Fig. 7 there seems to be a strong, compact component near the stellar continuum, which extends over ~250 pc (Lyα_i, hereinafter, F(Lyα) = 2.0×10^{-13} erg s^{-1} cm^{-2} not corrected for any kind of absorption), and another weaker and more diffuse emission over ~850 pc extending to the southwest direction (Lyα_{ii}, F(Lyα) = 2.8×10^{-14} erg s^{-1} cm^{-2}).

Table 8. X-ray spectral fitting.

Model	kT (keV) Norm[a]	Γ Norm[a]	Metallicity $Z_\odot$	ν	χ^2/ν
1: wabs*zwabs*mekal	0.81 2.9×10^{-5}	– –	0.5	16	3.486
2: wabs*zwabs*zpowerlw	– –	2.1 1.6×10^{-5}	–	16	2.947
3: wabs*zwabs*(mekal+zpowerlw)	$0.71^{+0.11}_{-0.10}$ $1.6^{+0.5}_{-0.5} \times 10^{-5}$	$1.8^{+0.3}_{-0.4}$ $9^{+3}_{-3} \times 10^{-6}$	0.5	14	1.083

Notes. [(a)] Units of normalization as in XSPEC. Hot plasma: $10^{-14}/\{4\pi[D_A(1+z)]^2\} \int n_e n_H dV$. Power-law: photons s^{-1} cm^{-2} keV^{-1} (1 keV).

In the spectral image along D2 direction displayed in Fig. 7 Lyα emission seems to be more complex, with regions of total absorption and total emission. Figure 7 shows the spatial profile along direction D2 of Lyα, being its value positive whenever it appears as emission and negative were it pure absorption. The UV stellar continuum from HST/STIS is superimposed to the Lyα-profile and a clear spatial detachment is observed between both emissions. Whereas the stellar continuum shows two peaks, one rather narrow due to the knot SE (~60 pc) and the other one more extended owing to knot NW (~150 pc), Lyα-profile is found in emission in three different regions: 1) northwest of knot NW, totally detached from the stellar continuum and extending over ≥600 pc (emission Lyα_{iii}, $F(\text{Ly}\alpha) = 1.8 \times 10^{-14}$ erg s^{-1} cm^{-2}), 2) within knot NW, <50 pc (emission Lyα_{iv}, $F(\text{Ly}\alpha) = 5 \times 10^{-15}$ erg s^{-1} cm^{-2}), and 3) northwest from knot SE and ~100 pc long (emission Lyα_v, $F(\text{Ly}\alpha) = 1.6 \times 10^{-14}$ erg s^{-1} cm^{-2}). While Lyα_{iii} shows a diffuse morphology, the Lyα_{iv} and Lyα_v contributions seem rather compact. However, the diffuse emission Lyα_{iii} although dimmer than the other two components, is the strongest one when integrated over its large extension, since it is observed up to the northwestern extreme of the slit. Hayes et al. (2007) found also in Haro 11 that the diffuse emission surrounding the stellar clusters is the most prominent contribution to L(Lyα). On the other hand, emission Lyα_{iv} is the weakest component, and unlike emissions Lyα_v and Lyα_{iii} it is fully located within one stellar knot.

3.4. X-rays

As explained in Sect. 2.2 the spectrum of the region labeled as NUCLEUS in Fig. 4 was analyzed. This region includes hard sources X1 and X2, with the former completely dominating the hard emission of NUCLEUS. Fitting of the spectrum was performed with XSPEC going from simpler to more complex models, evaluating the statistical significance of the change at each step through the F-test and considering it valid if probability significance was >99%. Galactic absorption was fixed to $N(\text{HI})_{\text{Gal}} = 6.3 \times 10^{19}$ cm^{-2}, whereas the intrinsic absorption was fixed to $N(\text{HI})_{\text{int}} = 7.0 \times 10^{19}$ cm^{-2} as derived by Lequeux et al. (1995). When freeing the hydrogen column density of the intrinsic absorption it was found that the result of the fit and the value of $N(\text{HI})_{\text{int}}$ did not change significantly, therefore we decided to fix it. For the metallicity we assumed the value $Z = Z_\odot/2$ obtained by Davidge (1989). The model which yielded a better fit is a composite of a hot plasma gas (hereinafter, HP, corresponding to the `mekal` model in XSPEC, Mewe et al. 1985) and a power-law emission (PL, in what follows) attenuated by both intrinsic and Galactic absorptions. HP would correspond to the diffuse soft emission filling the starbursting region and its surroundings, while the PL component is mostly dominated by X1. For the best fit achieved the temperature of the HP is $kT = 0.71^{+0.11}_{-0.10}$ keV and the PL index $\Gamma = 1.8^{+0.3}_{-0.4}$. No acceptable fit is obtained when considering only one single emitting component. Results assuming a Raymond-Smith model (`raymond` model in XSPEC, Raymond & Smith 1998) for the HP instead of `mekal` yielded similar results.

Other options were tested, like fitting the spectrum with a two-temperature hot plasma, but large uncertainties were obtained for the higher temperature. Also, metal abundances were freed after modeling the HP with `vmekal` (Mewe et al. 1985), obtaining best fits when O and Mg abundances were $Z(O)/Z(O)_\odot \sim 2.5$ and $Z(Mg)/Z(Mg)_\odot \sim 4$. However these models led to values of the reduced chi-squared of $\chi^2/\nu \sim 0.7$, which indicates an overparameterization of the fitting and were therefore rejected. On the other hand, as explained by Ott et al. (2005), α-elements are injected into the gas surrounding the stellar clusters by Type II SNe, whereas iron is mainly yielded into the ISM by Type I SNe, causing a time delay between both enrichments due to the different evolution of both types of stars producing each class of supernova. This causes a supersolar value of the ratio $Z(\alpha)/Z(\text{Fe})$ in the gas inside bubbles blown by starbursts which have been enriched by supernovae yields. This effect was modeled by Silich et al. (2001), who predicted an oversolar abundance of O compared to Fe during more than 40 Myr after the onset of the starburst. In order to study the overabundance of α-elements inside the hot gas we followed the procedure by Martin et al. (2002): the HP emission was modeled by `vmekal`, He was fixed to the nebular abundance, Mg, Ne, Si and Ca were linked to the O abundance which was freed (considered to be the α-group, $Z(\alpha)$), and the rest of the metals abundances were fixed to Fe abundance which was also left free (Fe group, Z(Fe)). However, no statistically significant improvement in the fit was obtained. We studied the inclusion of S and Ar into the α-group as Grimes et al. (2005) and Kobulnicky & Martin (2010) did, but very similar results were obtained.

The final results of the X-ray spectral fitting are shown in Table 8. Table 9 contains the X-ray luminosities for the best fitting model (Model 3), as well as the ratio of the contribution of the PL component over the HP one in the soft X-ray luminosity $L_{0.4-2.4\,\text{keV}}$. Finally Fig. 8 shows the X-ray spectrum of Haro 2 together with Model 3. Table 8 lists the values of the temperature kT of the HP, the PL index Γ, the metallicity of the gas assumed, the number of degrees of freedom ν and the reduced chi-squared χ^2/ν. Errors correspond to a confidence level of 90%. Stevens & Strickland (1998) obtained a lower temperature value $kT = 0.36$ keV when analyzing the ROSAT/PSPC observation of Haro 2. They assumed a very low metallicity $Z \sim Z_\odot/10$ and obtained a higher intrinsic hydrogen column density of $N(\text{HI}) = 2.2 \times 10^{21}$ cm^{-2} with very high uncertainties, which

Table 9. X-ray fluxes and luminosities.

Model	$F_{0.4-2.4\,\mathrm{keV}}{}^{a}$ (erg s^{-1} cm^{-2})	$F_{2.0-10.0\,\mathrm{keV}}{}^{a}$ (erg s^{-1} cm^{-2})	$L_{0.4-2.4\,\mathrm{keV}}{}^{b}$ (erg s^{-1})	$L_{2.0-10.0\,\mathrm{keV}}{}^{b}$ (erg s^{-1})	$(L^{\mathrm{PL}}_{0.4-2.4\,\mathrm{keV}}/L^{\mathrm{HP}}_{0.4-2.4\,\mathrm{keV}})^{b}$
3: wabs*zwabs*(mekal+zpowerlw)	$4.6^{+1.0}_{-1.1}\times10^{-14}$	$3.1^{+1.7}_{-1.5}\times10^{-14}$	$2.4^{+0.5}_{-0.6}\times10^{39}$	$1.5^{+0.8}_{-0.8}\times10^{39}$	$1.2^{+0.4}_{-0.5}$

Notes. [(a)] Values of fluxes have not been corrected for neutral absorption. [(b)] Values of luminosities have been corrected for neutral absorption.

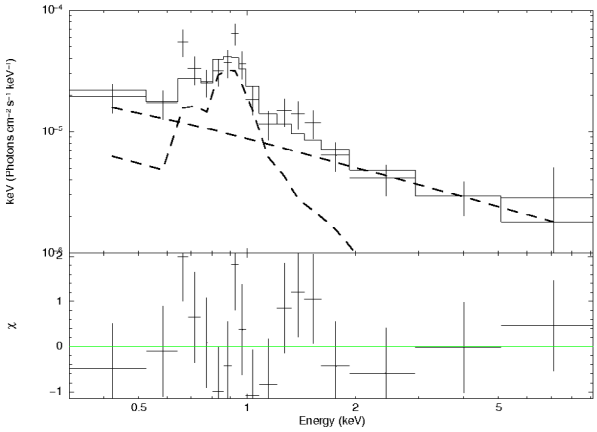

Fig. 8. X-ray spectrum of Haro 2 with the best fitting model (Model 3 in Table 8). Thermal and power-law components are shown in dashed lines. Fitting residuals are also shown in the *bottom panel*.

might explain the disagreement. On the other hand the value we obtained in our study for kT is similar to the values found in other star-forming galaxies. For instance, Summers et al. (2004) obtained a value of $kT = 0.75$ keV for the hotter component in their two-temperature composite hot plasma when fitting the soft X-ray emission of NGC 5253, and Martin et al. (2002) obtained $kT = 0.7$ keV for the component of the disk in the dwarf starbursting galaxy NGC 1569. Hayes et al. (2007) and Grimes et al. (2007) obtained $kT = 0.69$ keV and $kT = 0.68$ keV for Haro 11, respectively, and Grimes et al. (2005) and Kobulnicky & Martin (2010) calculated $kT = 0.60$ keV and $kT = 0.63$ keV for He 2-10, respectively. However, these values are relatively high when compared to the study by Strickland et al. (2004), who obtained $kT = 0.11$ keV and $kT = 0.37$ keV for a two-temperature model fitted simultaneously to eight starbursts whose X-ray point-sources had been removed. Also, Grimes et al. (2005) only found two sources with $kT > 0.5$ keV among seven dwarf starbursts. The kT value we propose for Haro 2 agrees better with the values found by Grimes et al. (2005) for their sample of ULIRGs.

As previously said, hard emission in Haro 2 is dominated by the point-like source X1. Attending to Persic & Rephaeli (2002) main contributors to the hard X-ray energy range 2–15 keV in starburst galaxies are high-mass X-ray binaries (HMXB) accreting gas onto a compact object. The great spatial resolution of *Chandra* enabled Strickland & Heckman (2007) to extract the composite spectrum of the detected X-ray point sources in the nuclear starbursting region of M82 (excluding M82 X1 identified as an ultraluminous X-ray source). After fitting the hard energy range using a power law they obtained $\Gamma \sim 1.0$. Similar values were found by Shaw Greeening et al. (2009) for 18 objects in M31 ($\Gamma = 0.8-1.2$). However, the fitting of Haro 2 X-ray spectrum points toward a photon index value of $\Gamma \sim 1.8$ for X1. Even more, the X-ray luminosity of X1 ($L_{0.4-10.0\,\mathrm{keV}} = 2.7\times10^{39}$ erg s^{-1}) is too large for a HMXB, and rather classifies it as an ultraluminous X-ray source (ULX), a type of hard-X-ray-emitting object with $L_{2.0-10.0\,\mathrm{keV}} \geq 10^{39}$ erg s^{-1} and Γ values in the range 1.6–2.2 (Colbert et al. 2004). Several of these sources have been highly studied in nearby galaxies where they can be spatially separated from the surrounding components by *Chandra*. Kaaret et al. (2001) and Matsumoto et al. (2001) reported the observation of the ULX M82 X-1, a compact, hard X-ray emitter within the local starbursting galaxy M82 and 170 pc far from its dynamical center. They found that its total X-ray luminosity is $L_X > 10^{40}$ erg s^{-1} and Matsumoto et al. (2001) calculated that the probability of this source being a background AGN is <1%. When fitted with an absorbed power law Kaaret et al. (2006) obtained a photon index $\Gamma = 1.67$ for this ULX. Kong et al. (2007) analyzed another hard, compact source in M82 labelled as X42.3+59 only ∼5″ (∼90 pc) away from M82 X-1. They also identified it as an ULX and they reported $\Gamma = 1.3-1.7$ and $L_{2.0-10.0\,\mathrm{keV}} = (7.8-11)\times10^{39}$ erg s^{-1}. Even more, Strickland et al. (2001) analyzed the X-ray emission of the starburst galaxy NGC 3628, finding a compact object ∼20″ (∼1 kpc) away from the nucleus. They obtained that the model which best fitted the X-ray emission of the object was an absorbed power law, finding $\Gamma = 1.8$ and $L_{0.3-8.0\,\mathrm{keV}} = 1.1\times10^{40}$ erg s^{-1}. Grimes et al. (2007) also suggested that the hard, intense X-ray emitter they found analyzing a *Chandra* image of Haro 11 (also a local Lyα-emitting starburst galaxy as Haro 2), could be an ULX, with a photon index $\Gamma = 1.6$ and a luminosity of $L_{0.3-8.0\,\mathrm{keV}} = 2.2\times10^{39}$ erg s^{-1}. Indeed, the X-ray luminosity $L_{0.4-10.0\,\mathrm{keV}} = 2.7\times10^{39}$ erg s^{-1} and the photon index $\Gamma \sim 1.8$ provided by the X-ray spectral fit of Haro 2 point toward X1 being an ULX, rather than an ordinary HMXB.

Strickland & Heckman (2007) found another source of hard X-rays in the star-forming nucleus of M82. After removing the point sources of the region they identified a diffuse hard X-ray component showing spectral features clearly different to the composite spectrum of the point sources removed and which extends along the plane of M82. They identified this component as the wind fluid driving the superwind of the galaxy, emitting as much as $L_{2.0-8.0\,\mathrm{keV}} = 4.4\times10^{39}$ erg s^{-1}, and produced by the collimation of the massive stellar winds and SN ejecta of the newly formed masive stars. This emission can be spectrally fitted in the hard X-rays range either with a Bremsstrahlung thermal model ($kT \sim 3-4$ keV), or with a power law with $\Gamma > 2.0$ yielding similar results. Nevertheless, we conclude that a wind fluid can not be responsible for the observed hard X-ray emission in Haro 2 since the latter is unresolved, and it basically appears associated to X1. We rather argue that X1 is most likely an ULX similar to the ones identified in other star-forming galaxies given the similarities in the values of its luminosity and photon index.

4. Discussion

The analysis of the observational data we have discussed in previous sections indicates that the nucleus of Haro 2 has experienced very recent star formation, being dominated by a population of massive stars with ages in the range 3.5–5 million years

and a total mass of $\sim 4 \times 10^6\ M_\odot$. The ISM seems to be heavily distorted, with a patchy distribution of dust clouds which blocks most of the UV continuum emitted by a high fraction of these stars, which are identified only by their contribution to the ionization of the gas and the heating of the dust particles. Moreover, while Haro 2 is surrounded by a relatively dense cloud of neutral gas, parts of it have been accelerated by the release of mechanical energy by these powerful starbursts, opening kinematical holes which allow the escape of Lyα photons out of the ionized regions, albeit in the form of P Cyg profiles. The release of mechanical energy has also led to powerful, diffuse soft X-ray emission around the central star-forming knots. Even more, Haro 2 presents a strong hard X-ray emission of the order of the soft X-ray emission, that is dominated by a single, unresolved source which is an ULX candidate. Finally, an extended and diffuse component of Lyα emission has been detected whose origin is unclear. This diffuse emission is spatially not correlated either with the UV continuum, nor even with the Balmer lines emission or Balmer decrement, but on the other hand it might originate close to the soft X-ray emitting regions.

4.1. Past star formation episodes

Previous episodes of massive star formation should have contributed to the chaotic structure of gas and dust in the nucleus of Haro 2. Some authors claim indeed that star formation has taken place in Haro 2 previously to the current starbursting episodes. Fanelli et al. (1988) studied signature lines of stars of different spectral types in spectra taken by the IUE. They found that the presence of O7-B0 V stars in Haro 2 reveals a young burst in the galaxy having ocurred within the past 10 Myr. However, due to the presence of A-type stars, they also argued that Haro 2 must have experienced two previous starburts, the most recent having ended less than 20 Myr ago. From this data, Summers et al. (2001) claimed that the star formation history of Haro 2 is composed of a recent burst with age ~5 Myr, another of 20 Myr, and a previous one which took place around 500 Myr ago. Also, they found that the older the burst, the larger the number of stars produced, and hence they concluded that the intensity of the episodes of the star formation must have decreased with time, maybe due to the lack of gas available for star production.

In order to check the presence of past star-forming episodes we used the models by Martín-Manjón et al. (2008) which combine codes of evolutionary population synthesis models, chemical evolution and photoionization to model the intensity of optical nebular lines, magnitudes and abundances of metals in a star-forming region. The models assume a history of star formation composed of bursts equally-separated, attenuated in time and corrected for the efficiency of the stellar production from the available gas. The production of stars from gas which has been chemically enriched by stellar winds and supernovae is consistently considered, as well as the effect of this enrichment on the intensity of nebular lines produced by photoionization. Our aim was to use the models to check whether previous star formation episodes are needed to reproduce the integrated intensity of the emission nebular lines measured by Moustakas & Kennicutt (2006). Lines observed in the spectrum and whose intensities are predicted by Martín-Manjón et al. (2008) are: O[II]3727, O[III]5007, O[I]6300, Hα, N[II]6584, S[II]6716 and S[II]6731. Intensity is scaled to Hβ and observed lines were corrected for stellar absorption and Galactic and intrinsic extinction. Since $L(\mathrm{H}\alpha)/L(\mathrm{H}\beta) \sim 2.86$ was assumed to correct for internal extinction we did not include Hα in the analysis to avoid biases toward models showing similar values.

Given the integrated value measured by Moustakas & Kennicutt (2006) for Haro 2 $EW(\mathrm{H}\beta) = 44$ Å, we only considered models with predicted $EW(\mathrm{H}\beta)$ in the range $34\ \text{Å} \leq EW(\mathrm{H}\beta) \leq 54\ \text{Å}$. Models consider bursts equally-separated in time by either 0.05, 0.1, 0.5 and 1.3 Gyr. Results show that models which best reproduce the intensity values of the lines are those 1) having had previous star formation bursts, either each 0.5 Gyr or 1.3 Gyr, and 2) last burst having taken place 3–5 Myr ago. Point 2) agrees with the ages of the bursts we have calculated, whereas point 1) reinforces the idea by Fanelli et al. (1988) and Summers et al. (2001) that intense star formation in Haro 2 took place as much as hundreds of millions of years before the current episode. Therefore these results confirm that previous star formation in Haro 2 occurred and is responsible for some of the features observed in the optical spectrum.

4.2. X-rays

Soft X-ray emission in a starburst is expected to be produced by 1) the heating of the diffuse gas surrounding the stellar clusters up to temperatures of millions of Kelvin, due to the stellar winds and supernovae injecting mechanical energy into the medium; and 2) by the emission of supernova remnants (SNRs) during the adiabatic phase. The contribution by the direct emission of individual stars is negligible when compared to the previous components (Cerviño et al. 2002). Evolutionary population synthesis models CMHK02 predict the soft X-ray emission of a starburst after defining the physical properties of the burst. CMHK02 model the component 1) through a Raymond-Smith plasma with $kT = 0.5$ keV, considering that a fraction ϵ_{xeff} from the mechanical energy is finally converted into X-ray luminosity. Typically, values $\epsilon_{\mathrm{xeff}} = 1$–$10\%$ are found for star-forming objects (Summers et al. 2001, 2004; Mas-Hesse et al. 2008). On the other hand, the soft X-ray emission by SNRs is considered to be due to the reversed shock which heats the gas inside the shell and which is modeled by a composite of three Raymond-Smith plasmas with $kT = 0.23$, 0.76, and 1.29 keV. See Cerviño et al. (2002) for a more detailed description.

As already explained, using the ROSAT/PSPC observation of Haro 2 Stevens & Strickland (1998) obtained values $kT = 0.36$ keV for the temperature of the hot plasma and $N(\mathrm{HI}) = 2.2 \times 10^{21}\ \mathrm{cm}^{-2}$ for the absorption, which yielded a higher soft luminosity $L_{\mathrm{ROSAT}} \sim 1.4 \times 10^{40}\ \mathrm{erg\,s}^{-1}$ when they assumed $Z \sim Z_\odot/10$. Summers et al. (2001) argued that the high uncertainties obtained for $N(\mathrm{HI})$ by Stevens & Strickland (1998) caused also large uncertainties in the X-ray luminosity, which was constrained in the range $L_{\mathrm{ROSAT}} \sim 2 \times 10^{39}$–$1.4 \times 10^{42}\ \mathrm{erg\,s}^{-1}$ and took $L_{\mathrm{ROSAT}} \sim 2 \times 10^{39}\ \mathrm{erg\,s}^{-1}$ as valid. Summers et al. (2001) estimated the injection of mechanical energy into the medium per unit of time $\dot{E}_{\mathrm{K}}$ by two methods: 1) applying the model for starburst-driven outflows by Castor et al. (1975) and Weaver et al. (1977) assuming that the radius of the superbubble blown by the star-forming activity in Haro 2 is $R_{\mathrm{B}} = 1.1$ kpc; and 2) using the ratio $\dot{E}_{\mathrm{K}}/L_{\mathrm{bol}}$ from SB99 models, where L_{bol} was considered to be well represented by the observed far infrared luminosity $L_{\mathrm{FIR}} = 1.4 \times 10^{43}\ \mathrm{erg\,s}^{-1}$. After performing these calculations for several ages, they assumed the value $\dot{E}_{\mathrm{K}} = 1.2 \times 10^{41}\ \mathrm{erg\,s}^{-1}$ considering an age of the burst of 5.8 Myr. Thus, with their values of $\dot{E}_{\mathrm{K}}$ and L_{ROSAT} Summers et al. (2001) obtained $\epsilon_{\mathrm{xeff}} \sim 0.02$ for Haro 2.

We calculated the X-ray luminosity predicted by the CMHK02 models for a composite of two starbursts with the ages and masses found for Population 1 and Population 2 in

Sect. 3.2 and included in Table 7. Metallicity of the models was fixed to $Z = 0.008$ since it is the closest value to the observed one $Z \sim Z_{\odot}/2$ (Davidge 1989). As shown in Fig. 8 soft X-ray emission is not strictly due to gas heated by the starburst activity (HP component), but also by the X1 emission (PL component). Actually, as indicated in Table 9 soft X-ray emission due to HP is ∼45% of the total soft X-ray emission observed, i.e. gas heated by the starburst activity emitts $L_{0.4-2.4\,\mathrm{keV}} \sim 1.1 \times 10^{39}$ erg s^{-1}. CMHK02 can reproduce this soft X-ray luminosity value for the composite of the bursts explained assuming $\epsilon_{\mathrm{xeff}} = 0.004$, i.e. the efficiency in the conversion of mechanical energy injected into the ISM by SNe and stellar winds in Haro 2 into soft X-ray luminosity is ∼0.4%. Summers et al. (2001) found the much higher value of 2% since they did not subtract the emission of X1 from the total observed luminosity. If we consider that the whole total luminosity $L_{0.4-2.4\,\mathrm{keV}} \sim 2.4 \times 10^{39}$ erg s^{-1} is due to gas heated by the starburst activity as Summers et al. (2001) did, we obtain an efficiency of ∼1% which is in better agreement with their value. When calculating the efficiency ϵ_{xeff} for galaxies where no subtraction of the emission from compact, point-like emitters is possible (due to lack of spatial resolution, for instance), then comparison must be made with efficiency values obtained with the total soft X-ray luminosity. As explained, this is the case for the value reported by Summers et al. (2001). Given the uncertainties in the calculation of the X-ray luminosity predicted by the CMHK02 models and in the estimation of the contribution by X1 to the soft X-ray emission, the range $\epsilon_{\mathrm{xeff}} = 0.004$–$0.01$ should be assumed for the value of this efficiency in Haro 2.

4.3. Lyα emission

Starbursts in the nucleus of Haro 2 dominate the ultraviolet emission of the galaxy (mainly by massive stars in dust-free environments), as well as its ionizing power (by the most reddened young stars), which produces conspicuous nebular emission lines. The spatial profiles of the UV continuum and the Lyα and Hα emission lines along directions D1 and D2 are shown in Fig. 7, together with the observed ratios Lyα/Hα and Hα/Hβ. Also, the profile of the expected Lyα/Hα ratio is included, which was calculated assuming case B recombination with $T_{\mathrm{e}} = 10^4$ K and $n(\mathrm{e}) = 500$ cm^{-3} (Lyα/Hα = 8.7, Hα/Hβ = 2.87), applying the expected internal dust reddening as derived from the observed Hα/Hβ ratio, as well as the corresponding Galactic extinction. Values of signal-to-noise ratio larger than 3 were obtained in the profiles by lowering the spatial resolution of the emission lines data when needed. Specifically, the resolution in Hα/Hβ was lowered down to 2.5 arcsec pixel^{-1}, whereas Lyα/Hα was calculated for 0.5 arcsec pixel^{-1} and 1.0 arcsec pixel^{-1} for directions D1 and D2, respectively. As seen in the figure, the profiles of the UV continuum and the Hα emission line are tightly spatially correlated, as expected since the Balmer lines are mainly produced by the recombination of gas ionized by the young massive stars.

On the other hand, Lyα is not always spatially coupled to the stellar continuum, Balmer lines emission or Hα/Hβ ratio. While compact Lyα components Lyα_{i}, Lyα_{iv} and Lyα_{v} are located within (or close to) a Balmer-line-emitting region, diffuse emissions Lyα_{ii} and Lyα_{iii} appear in regions where the continuum and other lines are very weak. In what follows we will analyze these 2 sets of regions independently, since their origin is probably different. Lyα_{i}, Lyα_{iv} and Lyα_{v} are apparently produced by recombination in the gas ionized by the massive stellar clusters, but the variable conditions of the neutral gas surrounding these regions (mainly kinematics and column density) determine whether the emission can escape or not, and whether the line profile is kinematically distorted. The final result is the alternance of peaks and valleys observed in the Lyα spatial profile between knots SE and NW along slit D2 (see Fig. 7). We want to stress that this structure is not reflected in the spatial profile of Hα since this line is not affected by resonant scattering.

The Lyα emission identified in regions Lyα_{ii} and Lyα_{iii} shows strikingly different properties. First of all, the Lyα/Hα ratio is much higher in these areas than close to the stellar clusters (see Fig. 7). Ratios as high as Lyα/Hα = 3 and Lyα/Hα = 6 are reached along directions D1 and D2, respectively. These observed ratios are much larger than predicted applying case B and the reddening derived from the Balmer decrement, representing Lyα emission ∼3 and >100 times higher than expected, respectively. Furthermore, it is remarkable that along D2, Lyα/Hα is highest where Hα/Hβ also reaches its highest value (NW end of the slit), leading initially to reject the hypothesis that the relatively large Lyα/Hα values in the diffuse regions are originated simply by a low abundance of dust.

Diffuse Lyα emission similar to Lyα_{ii} and Lyα_{iii} has been found in other local Lyα-emitting galaxies. Hayes et al. (2005) found that 70% of the total Lyα radiation of the galaxy ESO338-IG04 is diffuse emission located in a halo surrounding the central regions and lacking strong stellar continuum. Furthermore, Hayes et al. (2007) concluded that 90% of the Lyα emission in Haro 11 is also diffuse and is located in a featureless halo, where Lyα flux is much higher than expected from recombination, when scaled from the observed Hα intensity. Atek et al. (2008) studied local values of the Lyα/Hα ratio in a sample of local Lyα-emitting starburst galaxies. Together with the values found by Hayes et al. (2005) and Hayes et al. (2007) for ESO338-IG04 and Haro 11 respectively, they reported those for IRAS 0833 and NGC 6090. For the latter sources Atek et al. (2008) also found Lyα emission values higher than predicted from case B recombination considering the Hα fluxes observed, when applying the extinction derived from the Balmer decrement (Hα/Hβ).

These properties indicate that the origin of the Lyα emission in the diffuse regions is apparently different from that of the compact knots dominated by the massive clusters. We postulate that the Lyα emission in these diffuse regions could be enhanced with respect to Hα either by an additional emission component, associated to the hot plasma identified in the X-ray image, by leaking of the Lyα photons created in the ionized regions, after multiple scattering within the neutral clouds, by reflection on a dust screen, or by a combination of the 3 processes. In the next subsections we describe in some detail these different, non-exclusive models.

4.3.1. Photoionization by the hot plasma

For this model we assumed that the Lyα diffuse emissions Lyα_{ii} and Lyα_{iii} in Haro 2 have been produced by ionization dominated mainly by the hot plasma responsible for the intense soft X-ray radiation, and not by the massive stellar clusters as for Lyα_{i}, Lyα_{iv} and Lyα_{v}. As we observe in Fig. 4 there seems to be some spatial correlation between the diffuse Lyα components and the diffuse, soft X-ray emission, originated by the heating in shock fronts of the interstellar gas surrounding the stellar clusters. We postulate that this X-ray radiation might have ionized the nebular gas in these regions, in an environment far from case B recombination conditions.

To check this possibility we used the photionization code CLOUDY 10.00 (Ferland et al. 1998). Ratios Hα/Hβ and Lyα/Hα were calculated in two extreme cases in which a

spherical cloud of gas is ionized by a central source, which is a massive star in Model 1, and a hot plasma in Model 2. In the former we modeled the continuum with a Kurucz star with $T \sim 4 \times 10^4$ K and emitting $Q(H) = 10^{50}$ s^{-1} ionizing photons, whereas the electronic density was assumed to be $n(\mathrm{e}) = 10^3$ cm^{-3}. Given a typical distance between the star and the cloud of gas of ∼1 pc, the value of the ionization parameter is $U = 0.1$. On the other hand, for Model 2 we assumed a Bremsstrahlung emission with $T = 10^7$ K and $n(\mathrm{e}) = 10^3$ cm^{-3}, keeping the ionization parameter within $U = 10^{-8}$–10^{-5}. This extreme conditions were chosen to reproduce the physical properties of high-density filaments compressed by the shock fronts.

The emission line ratios computed for Model 1 are $(\mathrm{H}\alpha/\mathrm{H}\beta)_{\mathrm{Model\,1}} = 2.9$ and $(\mathrm{Ly}\alpha/\mathrm{H}\alpha)_{\mathrm{Model\,1}} = 10.1$, indeed very similar to the predictions of the standard case B, as expected. On the other hand, for Model 2 we obtained $(\mathrm{H}\alpha/\mathrm{H}\beta)_{\mathrm{Model\,2}}$ in the range 3.0–4.0, and $(\mathrm{Ly}\alpha/\mathrm{H}\alpha)_{\mathrm{Model\,2}}$ from 7.0 to 12.0. It is important to note that Model 2 predicts systematically higher $\mathrm{H}\alpha/\mathrm{H}\beta$ values than case B. This implies that if the contribution by the hot plasma is important, we could overestimate the abundance of dust if derived assuming case B conditions.

We would expect a physical scenario with a smooth transition from Model 1 to Model 2 conditions as we move away from the vicinity of the massive clusters to more external regions. Figure 7 shows compact Lyα emission, if any, close to the stellar clusters in Haro 2. Assuming that Model 1 conditions prevail in these regions, reddening correction as derived from the case B $\mathrm{H}\alpha/\mathrm{H}\beta$ ratio should be applied. The $\mathrm{Ly}\alpha/\mathrm{H}\alpha$ ratios observed around these regions are generally lower than expected from case B, even taking into account the effect of reddening. This is especially noticeable around $\mathrm{Ly}\alpha_{\mathrm{iv}}$ and $\mathrm{Ly}\alpha_{\mathrm{v}}$. We know already from UV spectroscopy that scattering in the outflowing neutral gas surrounding knot SE, together with the relatively high dust abundance (as derived from the observed $\mathrm{H}\alpha/\mathrm{H}\beta$ ratio), are responsible for the low escape fraction of the Lyα photons originated on this area.

On the contrary, the diffuse Lyα emission is originated in regions spatially separated from the stellar clusters, where the ionization might be dominated by the hot plasma. Since Model 2 predicts higher intrinsic $\mathrm{H}\alpha/\mathrm{H}\beta$ ratios than Model 1, the extinction derived in the diffuse emitting regions would be much lower than assuming case B, allowing for higher Lyα escape fractions in these areas. The ratio measured on $\mathrm{Ly}\alpha_{\mathrm{ii}}$, $\mathrm{Ly}\alpha/\mathrm{H}\alpha < 3.0$, is compatible with the results found by Mas-Hesse et al. (2003). They found that the diffuse Lyα emission exhibits a clear P Cyg profile all along slit D1, at any distance from the stellar knot SE. This implies that a significant fraction of the emitted Lyα photons (the blue wing of the line) has been affected by resonant scattering, decreasing the outcoming line flux in this area. On region $\mathrm{Ly}\alpha_{\mathrm{iii}}$, both the observed $\mathrm{H}\alpha/\mathrm{H}\beta$ and $\mathrm{Ly}\alpha/\mathrm{H}\alpha$ ratios could be consistent with the presence of shock-heated filaments, with small or none attenuation by dust. Indeed, the strong X-ray flux in this area would most likely destroy most of the dust particles. The fact that the $\mathrm{Ly}\alpha/\mathrm{H}\alpha$ ratio is very close to the intrinsic predictions by Model 2 requires also that the medium in front of this region is transparent to Lyα photons: either the column density of neutral gas is small enough, or it is outflowing with a projected velocity large enough not to affect the Lyα intensity ($v_{\mathrm{out}} \geq 400$ km s^{-1}). Unfortunately the spectral resolution is not enough to analyze the spectral profile of $\mathrm{Ly}\alpha_{\mathrm{iii}}$.

Model 2 predicts $L(\mathrm{H}\alpha)/L_{0.4-2.4\,\mathrm{keV}} \sim 10^{-3}$–$10^{-2}$, where $L(\mathrm{H}\alpha)$ and $L_{0.4-2.4\,\mathrm{keV}}$ are the intrinsic Hα luminosity produced and the ionizing soft X-ray luminosity emitted by the hot plasma, respectively. We measured $L(\mathrm{H}\alpha)/L_{0.4-2.4\,\mathrm{keV}}$ in both the regions dominated by the stellar clusters and those showing diffuse Lyα emission. For the compact regions we found $L(\mathrm{H}\alpha)/L_{0.4-2.4\,\mathrm{keV}} \sim 300$, while in the diffuse regions, far away from the stellar clusters, $L(\mathrm{H}\alpha)/L_{0.4-2.4\,\mathrm{keV}} \sim 1$. This severe decrease in the $L(\mathrm{H}\alpha)/L_{0.4-2.4\,\mathrm{keV}}$ ratio when moving toward regions showing diffuse emission reinforces the idea of ionization in these sites being dominated by the hot plasma itself. Values of $L(\mathrm{H}\alpha)/L_{0.4-2.4\,\mathrm{keV}} \sim 10$–$100$ are measured in the intermediate regions, where the ionizing flux of the massive stars increases with respect to the hot plasma one as we move closer to the stellar clusters. Although the measured $L(\mathrm{H}\alpha)/L_{0.4-2.4\,\mathrm{keV}}$ is always higher than the absolute values predicted by Model 2, we should be aware that the hot plasma filaments which are expected to ionize the local surrounding medium can not be resolved, and hence the flux values and ratios obtained are average values. Measuring $L(\mathrm{H}\alpha)/L_{0.4-2.4\,\mathrm{keV}}$ locally would require a higher spatial resolution and better statistics in the X-ray observation. However, the observed trend in $L(\mathrm{H}\alpha)/L_{0.4-2.4\,\mathrm{keV}}$ does point toward the diffuse Lyα emission being produced by the ionization caused by the hot plasma, whereas the compact Lyα emission is consistent with being originated in the gas ionized by the massive stars.

Finally, while the simulations with CLOUDY suggest that the hot plasma could dominate the Lyα emission in the external regions of Haro 2, we have not been able to reproduce all the spectral features observed in the regions showing $\mathrm{Ly}\alpha_{\mathrm{ii}}$ and $\mathrm{Ly}\alpha_{\mathrm{iii}}$ emissions. Whereas the ionizing hot plasma models, combined with some attenuation, can reproduce the observed ratios $\mathrm{Ly}\alpha/\mathrm{H}\alpha$, $\mathrm{H}\alpha/\mathrm{H}\beta$ and $L(\mathrm{H}\alpha)/L_{0.4-2.4\,\mathrm{keV}}$, the predictions for some other lines (like Fe II 4300 and Fe II 6200) are overestimated when compared with the observations. Furthermore, other lines present in the spectra such as O[II]3727 and O[III]4959, 5007 are underestimated by these models. Nevertheless, we want to stress that our models are based on a simplistic scenario assuming spherical geometry, while X-ray-emitting filaments should be significantly more complex in shape, structure and physical conditions. A more detailed modeling of the geometry of these filaments is out of the scope of this work. We want to retain here only the idea that a very hot, X-ray-emitting plasma could generate an additional Lyα emission component under conditions that would differ significantly from case B ones, and which might be the major contributor to the diffuse Lyα emission in Haro 2.

4.3.2. Scattering by the neutral gas

As we have already discussed, Lyα photons are resonantly scattered by neutral hydrogen atoms. Verhamme et al. (2006) have modelled the properties of Lyα radiation transfer through a neutral medium, assuming different conditions of dust abundance, kinematics of the gas, column density, ... In the absence of dust, Lyα photons could travel long distances through the neutral cloud, before leaking from its surface, escaping from the galaxy. Nevertheless, the multiple scattering would at least modify their distribution in energy, leading to a two-peak emission profile with almost no emission at the central wavelength. If the gas has some velocity with respect to the ionized region where the Lyα photons were produced, a P Cyg-like profile would be expected. The multiple scattering increases the mean free path of the photons through the neutral cloud, increasing the probability of being absorbed by dust.

The presence of neutral gas around the Haro 2 nuclear starburst is evident from the observations. The P Cyg profile of the Lyα emission line along slit D1 indicates that a least knot SE is surrounded by outflowing neutral gas. The regions where

the Lyα emission disappears completely along slit D2 are most likely also covered by neutral gas clouds, in different kinematical states. Therefore, it might be possible that the Lyα photons, formed in the ionized regions close to the stellar clusters, but being scattered by these neutral clouds, end up leaking at relatively large distances. Since Hα would not be affected by this process, the net result would be an enhancement of the Lyα emission on extended areas far away from the ionized regions, as proposed by Hayes et al. (2007), which in principle would be consistent with the observations. However, in that case the Balmer lines would be produced by the ionizing flux originated in the stellar clusters, and conditions similar to case B would apply. The observed Hα/Hβ values would indicate a high abundance of dust particles in front (or mixed with) the clouds surrounding Ly$\alpha_{\rm ii}$ and Ly$\alpha_{\rm iii}$ regions, and they would most likely destroy most of the scattered Lyα photons. Nevertheless, while the Lyα photons would be leaking from the surface of the neutral clouds, the residual Balmer lines emission in these regions would probably be originated at a different location, so that the relatively high extinction derived from the Hα/Hβ ratio would not apply to the Lyα emission. A detailed analysis of the Lyα spectral profile of the Ly$\alpha_{\rm iii}$ region, not possible with the low-resolution existing data, would be required to compare it with the predictions of radiation transfer models.

4.3.3. Dust reflection

If we do not consider the possible contribution to ionization by the hot plasma, and assume that conditions close to case B apply over most of the nuclear region of Haro 2, then the high Hα/Hβ ratios (especially on region Ly$\alpha_{\rm iii}$) would point to the presence of dense dust clouds or filaments at certain distance from the stellar clusters. These dust clouds could be reflecting the emission originated close to the starburst knots. Since UV photons are more efficiently dispersed than optical photons, an enhancement of the Lyα emission over the Balmer lines in these regions would be naturally produced, explaining the higher Lyα/Hα ratios in these extended regions. In principle we would expect also Hα/Hβ < 2.86 in these regions, but since dispersion would be so much efficient for Lyα wavelengths than for Hα or Hβ, it might be well that the observed Hα and Hβ emissions are dominated by the component originated locally, and therefore attenuated by the local dust. The local Lyα would be almost totally destroyed, as expected from the high $E(B-V)$ derived. But the reflected Lyα component (scattered at the surface of the dust clouds, and therefore not affected by the internal extinction) could be strong enough to produce the observed Lyα/Hα values.The main flaw of this model is that it predicts lower Lyα equivalent widths than observed, since the UV continuum would also be reflected.

These different mechanisms are not mutually exclusive, and each of them could be contributing to a different extent to the Lyα emission detected in starburst galaxies like Haro 2. Scarlata et al. (2009) proposed indeed a scenario which combines both the scattering by neutral gas and the reflection by dust clouds, based on a clumpy distribution of neutral clouds rich in dust, surrounding the ionized region. While the Balmer lines and the UV continuum would be attenuated by the dust particles along the line of sight, scattering and/or reflection at the surface of the neutral clouds would allow the Lyα photons to find their way through the medium with a rather high efficiency, leading to high Lyα/Hα ratios when observed globally. They argued that this scenario could explain the integrated values of Lyα/Hα = 1–5 measured in a sample of GALEX Lyα-emitters at z = 0.18–0.28. Mapping the distribution of the dust clouds in Haro 2 with very high spatial resolution would be needed to verify if this scenario could explain the diffuse Lyα emission.

However, we argue that ionization by the hot plasma is the dominating source responsible for the diffuse emission in Haro 2. Despite the limitations of this model concerning the predicted intensities of some emission lines, it can naturally explain the spatial coupling of the Ly$\alpha_{\rm ii}$ and Ly$\alpha_{\rm iii}$ components with the soft X-ray emission, the measured values of the Lyα/Hα and L(Hα)/$L_{0.4-2.4\,\rm keV}$ ratios and the high escape fraction of Lyα photons from regions with high Hα/Hβ ratios.

If the diffuse Lyα emission detected in Haro 2 and other starburst galaxies is originated by ionization by hot plasma, and not directly by the massive stars, the use of Lyα could overestimate the star formation rate in galaxies at hight redshift by a significant factor (when integrated over the whole galaxy, Hayes et al. (2005, 2007) found that the diffuse emission is a dominant fraction of the total Lyα emission observed). This adds to the difficulty of determining the escape fraction of Lyα photons originated directly by stellar ionization along the history of the Universe (Hayes et al. 2011). A further correction should be applied to the procedure used to convert Lyα luminosity into number of ionizing photons, and thus star formation rate. Calibrating the strength of these corrections requires a detailed analysis of a larger sample of Lyα-emitting starburst galaxies in the local Universe.

5. Conclusions

We have carried out a complete multiwavelength spectral and photometric analysis of the star-forming nucleus of the local Lyα-emitter Haro 2, focusing on the Lyα emission and its relation with different starburst-related parameters. UV, optical, NIR and X-ray images, as well as UV-optical spectral observations with high spatial and spectral resolution, have been analyzed.

- We have characterized the starburst of Haro 2 by comparison with evolutionary population synthesis models, reproducing the UV, Hα and FIR luminosities values as well as the properties of the SiIV and CIV stellar absorption lines. We have identified a population of young massive stars (ages ~3.5–5.0 Myr) with a total stellar mass $M \sim 4\times10^6\ M_\odot$ (for an IMF with mass limits of 2–120 $M_\odot$), and whose continuum is affected by a differential extinction with $E(B-V)$ values in the range $E(B-V) = 0.035- \geq 0.5$. Stars located in dust-free regions dominate the UV emission, whereas those within dust-rich clouds are completely obscured in the UV, but are the main contributors to the Hα and FIR luminosities of the galaxy.
- We have identified a diffuse soft X-ray emission extended over the whole nucleus. This component is attributed to the gas heated by the release of mechanical energy by the stellar winds and supernovae from the starburst, as well as to supernova remnants. We have estimated that ~0.4–1% of the mechanical energy injected is converted into soft X-ray emission, which is a typical value for this kind of sources. A hard, unresolved X-ray emission is located on the SE star-forming knot, apparently originated by an UltraLuminous X-ray (ULX) source related to the starburst episode.
- Both compact and diffuse Lyα emission components, together with regions of total absorption, are observed along the major and minor axes of the star-forming nucleus of Haro 2. Intensities of the compact Lyα emission are lower

than those expected from Hα fluxes and case B recombination theory, considering dust extinction. On the other hand, the diffuse Lyα emission is stronger than expected from Hα, and extends over 850 pc and >600 pc along minor and major axes, respectively. We have found that the Lyα emission is spatially decoupled from the UV continuum, the Balmer lines emission and the Hα/Hβ ratio, but the diffuse Lyα component is apparently correlated with the diffuse soft X-ray emission.

- Outflowing of the neutral hydrogen surrounding the stellar clusters, energized by the starburst activity, enables Lyα photons from both compact and diffuse components to escape from Haro 2, leaving the signature of a clear P Cyg profile in the emission line. Nevertheless, the irregular distribution and kinematical properties of the expanding neutral gas lead the Lyα photons produced in recombination sites to escape only in certain regions. Hα photons are not affected at all by the kinematics of the neutral gas, and escape directly from all ionized regions. This explains the spatial decoupling between the Lyα and Hα compact emissions.
- Compact Lyα emission is produced by recombination in the gas ionized by the massive stellar clusters. The combined effect of resonant scattering by neutral gas and attenuation by dust, as traced by the P Cyg profiles and the high values of Hα/Hβ ratio respectively, decreases the escape fraction of the Lyα photons and yields observed fluxes below the case B recombination predictions.
- On the other hand, the diffuse Lyα emission has apparently a rather different origin. We argue that the shock fronts heated to X-ray emitting temperatures by the release of mechanical energy could ionize the surrounding nebular gas under conditions far from case B recombination, as suggested by the spatial correlation between the soft X-ray emission and the diffuse Lyα component. Simple modeling with CLOUDY reproduces indeed the Lyα/Hα, Hα/Hβ and $L(\mathrm{H}\alpha)/L_{0.4-2.4\,\mathrm{keV}}$ ratios measured in this region.
- Nevertheless, our results do not reject other physical processes proposed previously that could also contribute to enhance the intensity of the diffuse Lyα emission line. Lyα photons, though originated close to the massive stars, could be leaking from the surface of distant neutral clouds after multiple scattering within the gas, depending on its distribution and the abundance of dust. Moreover, under certain circumstances the dust clouds could even contribute to enhance the diffuse Lyα emission by differential reflection.

Acknowledgements. H.O.F. and J.M.M.H. are partially funded by Spanish MICINN grants CSD2006-00070 (*CONSOLIDER GTC*), AYA2010-21887-C04-02 (*ESTALLIDOS*) and AYA2008-03467/ESP. H.O.F. is funded by Spanish FPI grant BES-2006-13489. M.H. received support from the Agence Nationale de la Recherche (ANR-09-BLAN-0234-01). H.A. and D.K. are supported by the Centre National d'Études Spatiales (CNES) and the Programme National de Cosmologie et Galaxies (PNCG). We want to acknowledge the use of the *Starburst99* models and the NASA/IPAC Extragalactic Database (NED). We are very grateful to the ESTALLIDOS collaboration for its scientific support. Also, we thank Giovanni Miniutti for his useful comments on X-ray modeling of HMXBs. We are very grateful to Hervé Bouy for his help in creating Figs. 1, 3 and 5 and to Nuria Huélamo and Hervé Bouy for fruitful discussions about continuum subtraction and PSF issues. We also thank Ricardo Amorín for allowing us to show the NOT/ALFOSC image of Haro 2. We want to thank Mercerdes Mollá and Mariluz Martín-Manjón for their help on the use and interpretation of their models. We are also grateful to Valentina Luridiana and Sebastiano Cantalupo for giving us figures, data and insight on collisional excitation and recombination theory. This paper was based on observations with *Hubble* Space Telescope and *Chandra*.

References

Adamo, A., Östlin, G., & Zackrisson, E. 2010, MNRAS, 407, 870
Arnaud, K. A. 1996, in Astronomical Data Analysis Software and Systems V, eds. G. H. Jacoby, J. Barnes (San Francisco: ASP), ASP Conf. Ser., 101, 17
Atek, H., Kunth, D., Hayes, M., Östlin, G., & Mas-Hesse, J. M. 2008, A&A, 488, 491
Atek, H., Schaerer, D., & Kunth, D. 2009, A&A, 502, 791
Calzetti, D., Armus, L., Bohlin, R. C., et al. 2000, ApJ, 533, 682
Cardelli, J. A., Clayton, G. C., & Mathis, J. S. 1989, ApJ, 345, 245
Castor, J., McCray, R., & Weaver, R. 1975, ApJ, 200, L107
Cerviño, M., Mas-Hesse, J. M., & Kunth, D. 2002, A&A, 392, 19
Chandar, R., Leitherer, C., & Tremonty, C. A. 2004, ApJ, 604, 153
Chen, W. L., & Neufeld, D. A. 1994, A&A, 432, 567
Colbert, E. J. M., Heckman, T. M., Ptak, A. F., Strickland, D. K., & Weaver, K. A. 2004, ApJ, 602, 231
Davidge, T. J. 1989, PASP, 101, 494
Fanelli, M. N., O'Connell, R. W., & Thuan, T. X. 1988, ApJ, 334, 665
Ferland, G. J., Korista, K. T., Verner, D. A., et al. 1998, PASP, 110, 761
Gil de Paz, A., Madore, B. F., & Pevunova, O. 2003, ApJS, 147, 29
Grimes, J. P., Heckman, T., Strickland, D., & Ptak, A. 2005, ApJ, 628, 187
Grimes, J. P., Heckman, T., Strickland, D., et al. 2007, ApJ, 668, 891
Gronwall, C., Ciardullo, R., & Hickey, T. 2007, ApJ, 667, 79
Hayes, M., Östlin, G., Mas-Hesse, J. M., et al. 2005, A&A, 438, 71
Hayes, M., Östlin, G., Atek, H., et al. 2007, MNRAS, 382, 1465
Hayes, M., Östlin, G., Schaerer, D., et al. 2010, Nature, 464, 562
Hayes, M., Schaerer, D., Östlin, G., et al. 2011, ApJ, 730, 8
Helou, G., Soifer, B. T., & Rowan-Robinson, M. 1985, ApJ, 298, L7
Kaaret, P., Prestwich, A. H., Zezas, A., et al. 2001, MNRAS, 321, L29
Kaaret, P., Simet, M. G., & Lang, C. C. 2006, ApJ, 646, 174
Kobulnicky, H. A., & Martin, C. L. 2010, ApJ, 718, 724
Kong, A. K. H., Yang, Y. J., Hsieh, P.-Y., Mak, D. S. Y., & Pun, C. S. J. 2007, ApJ, 671, 349
Legrand, F., Kunth, D., Mas-Hesse, J. M., & Lequeux, J. 1997, A&A, 326, 929
Leitherer, C., Schaerer, D., & Goldader, J. D. 1999, ApJS, 123, 3
Lequeux, J., Kunth, D., Mas-Hesse, J. M., & Sargent, W. L. W. 1995, A&A, 301, 18
Maíz-Apellániz, J., Mas-Hesse, J. M., Muñoz-Tuñón, C., Vílchez, J. M., & Castañeda, H. O. 1998, A&A, 329, 409
Martin, C. L., Kobulnicky, H. A., & Heckman, T. M. 2002, ApJ, 574, 663
Martín-Manjón, M. L., Mollá, M., Díaz, A. I., & Terlevich, R. 2008, MNRAS, 385, 854
Mas-Hesse, J. M., & Kunth, D. 1999, A&A, 349, 765
Mas-Hesse, J. M., Kunth, D., Tenorio-Tagle, G., et al. 2003, ApJ, 598, 858
Mas-Hesse, J. M., Otí-Floranes, H., & Cerviño, M. 2008, A&A, 483, 71
Matsumoto, H., Tsuru, T. G., Koyama, K., et al. 2001, ApJ, 547, L25
Méndez, D., & I. Esteban, C. 2000, A&A, 359, 493
Mewe, R., Gronenschild, E. H. B. M., & van den Oord, G. H. J. 1985, A&AS, 62, 197
Moustakas, J., & Kennicutt R. C., Jr. 2006, ApJS, 164, 81
Osterbrock, D. E. 1989, Astrophysics of Gaseous Nebulae and Active Galactic Nuclei (California: University Science Books)
Östlin, G., Hayes, M., Kunth, D., et al. 2009, AJ, 138, 923
Otí-Floranes, H., & Mas-Hesse, J. M., 2010, A&A, 511, A61
Ott, J., Walter, F., & Brinks, E. 2005, MNRAS, 358, 1423
Persic, M., & Rephaeli, Y. 2002, A&A, 382, 843
Prévot, M. L., Lequeux, J., Prevot, L., Maurice, E., & Rocca-Volmerange, B. 1984, A&A, 132, 389
Raymond, J. C., & Smith, B. W. 1977, ApJS, 35, 419
Scarlata, C., Colbert, J., & Teplitz, H. I. 2009, ApJ, 704, L98
Shaw Greeening, L., Barnard, R., Kolb, U., Tonkin, C., & Osborne, J. P. 2009, A&A, 495, 733
Silich, S. A., Tenorio-Tagle, G., Terlevich, R., Terlevich, E., & Netzer, H. 2001, MNRAS, 324, 191
Stevens, I. R., & Strickland, D. K. 1998, MNRAS, 294, 523
Strickland, D. K., & Heckman, T. M. 2007, ApJ, 658, 258
Strickland, D. K., & Stevens, I. R. 1999, MNRAS, 306, 43
Strickland, D. K., Colbert, E. J. M., Heckman, T. M., et al. 2001, ApJ, 560, 707
Strickland, D. K., Heckman, T. M., Colbert, E. J. M, Hoopes, C. G., & Weaver, K. A. 2004, ApJS, 151, 193
Summers, L. K., Stevens, I. R., & Strickland, D. K. 2001, MNRAS, 327, 385
Summers, L. K., Stevens, I. R., Strickland, D. K., & Heckman, T. M. 2004, MNRAS, 351, 1
Tapken, C., Appenzeller, I., & Noll, S. 2007, A&A, 467, 63
Tenorio-Tagle, G., Silich, S. A., Kunth, D., Terlevich, E., & Terlevich, R. 1999, MNRAS, 309, 332
Verhamme, A., Schaerer, D., & Maselli, A. 2006, A&A, 460, 397
Weaver, R., McCray, R., Castor, J., Shapiro, P., & Moore, R. 1977, ApJ, 218, 377
Wilkins, S. W., Hopkins, A. M., Trentham, N., & Tojeiro, R. 2008, MNRAS, 391, 363